J. Fluid Mech. (2025), *vol.* 1016, A55, doi:10.1017/jfm.2025.10456

JFM PAPERS

Influence of free stream disturbance on hypersonic boundary layer dynamics over a cone–cylinder –flare

Anirudh Lakshmi Narasimha Prasad[1], **K.P. Sarath**[1] **and S. Unnikrishnan**[1]

[1]Department of Mechanical Engineering, FAMU-FSU College of Engineering, Florida State University, Tallahassee FL-32310, USA

Corresponding author: Anirudh Lakshmi Narasimha Prasad, al20di@fsu.edu

(Received 6 March 2025; revised 28 May 2025; accepted 6 July 2025)

Hypersonic transition studies on systems sustaining multimodal dynamics are critical to understanding aerothermal loading on flight-relevant configurations. The present work evaluates transition mechanisms in hypersonic boundary layers over a cone–cylinder–flare geometry, and its sensitivity to free stream disturbance amplitudes, using a global linear stability approach and direct numerical simulations (DNS). Under relatively quiet conditions, the flow field resembles the laminar solution, consisting of a large separation zone over the cylinder–flare junction. Linear analysis identifies multiple convective instabilities including, oblique first modes and two-dimensional second modes over the cone segment, and shear layer instabilities over the separation zone. This separation zone also supports a stationary global instability, producing streamwise streaks with an azimuthal wavenumber, $m = 21$, which eventually drives transition as captured in the DNS. Conversely, at higher disturbance amplitudes, the largely attached boundary layer transitions through a bypass mechanism, involving intermodal interactions between low-frequency streaks, and first mode instabilities. The resulting upstream shift in transition onset leads to a significant rise in both steady and unsteady surface loading. Peak thermal loading under quiet conditions displays the signature of the linear global instability over the flare, whereas that under noisier environments is dominated by an imprint of unsteady Görtler vortices over the cylinder–flare junction.

Key words: hypersonic flow, transition to turbulence, boundary layer receptivity

1. Introduction

Transition to turbulence in hypersonic boundary layers (HBLs) has a profound impact on aerodynamic performance, thermal management and structural durability of high-speed air vehicles. The intense surface loading that arises within transitional and turbulent boundary layers imposes considerable constraints on vehicle design, often diminishing propulsive efficiency and impacting vehicle longevity and operability (Guo *et al.* 2022; Zhou *et al.* 2022). Therefore, understanding the mechanisms that initiate and sustain boundary layer transition, and devising strategies to mitigate or delay it, is imperative. Sensitivity of transition to an expansive parametric space makes this an extremely difficult task. This includes, influence of free stream conditions (Goldstein 2014; Andrews & Poggie 2020), thermal boundary conditions (BCs) (Wannenwetsch & Martindale 1977; Araya *et al.* 2021; Unnikrishnan & Gaitonde 2021), geometric features (Stetson 1983; Paredes *et al.* 2018; Goparaju, Unnikrishnan & Gaitonde 2021), surface roughness (Schneider 2008; Shi *et al.* 2019) and the spectral and fluid-thermodynamic characteristics of the surrounding disturbance environment (Reshotko 1976; Balakumar & Chou 2018).

Extensive research has been performed to study fundamental mechanisms of hypersonic transition using canonical geometries, including, flat plates (Sivasubramanian & Fasel 2011; Unnikrishnan, Cavalieri & Gaitonde 2019), wedges (Balakumar 2015), circular cones (Chou *et al.* 2011) and, more recently, flared cones (Hader & Fasel 2019; Zhang & Shi 2022), double cones (Fan, Hao & Wen 2022) and cone–cylinder–flare (CCF) structures (Benitez *et al.* 2023*a*). While sharp flat-plate/straight-cone configurations are commonly utilized to research natural and controlled transition pathways, especially focusing on inherent instability modes, studies with flight-relevant geometries should expect added complexities. These include the impact of geometry-induced pressure gradients, nose-tip effects, the non-uniformity in base flow due to angle of attack and the strong viscous–inviscid interactions that substantially influence transition mechanisms. Such studies are necessary to extend our fundamental understanding of hypersonic transition to practical configurations, which may sustain interplay of multiple flow phenomena, that eventually determine realistic loading scenarios on the vehicle.

Using linear theory and scale-resolved simulations, the present work addresses the above necessity by studying the transitional and post-transitional dynamics, and wall loading over an idealized hypersonic geometry, which sustains multimodal mechanisms and their mutual interactions under certain operating conditions. Specifically, we study the flow dynamics over a CCF geometry inspired by the HIFiRE-1 experiments (Kimmel & Prabhu 2015), under relatively low and high free stream perturbation levels. This geometry originally featured a blunted 7° half-angle cone with an attached cylinder, and a 33° flare configuration (Adamczak, Alesi & Frost 2009). While the cone–cylinder junction produces an expansion fan, the cylinder–flare junction creates a compression corner, resulting in an oblique shock. Due to the associated adverse pressure gradient, the boundary layer thickens and decelerates. The degree of adverse pressure gradient and the intensity of the oblique shock are highly dependent on the turning angle, and can drive separation of the incoming boundary layer at sufficiently large angles. This generates a shock–boundary layer interaction (SBLI) zone and a separation bubble, over which a shear layer develops. When present, the separation bubble can accelerate the onset of transition in the shear layer, potentially driving the flow to a fully turbulent state before reattachment in certain configurations (Paredes *et al.* 2022). This idealized geometry thus facilitates a rigorous study of several fundamental multimodal interactions that may occur in hypersonic flight vehicles, some of which are further detailed below.

Early work by Becker & Korycinski (1962) on an ogive–cylinder–flare model discusses SBLI-induced separation bubbles, and the impact of boundary layer conditions on bubble geometry, underscoring a strong relationship between the separation region and transitional flow dynamics. Subsequently, Ginoux (1965) investigated the CCF geometry experimentally, identifying streamwise vortices on the flare downstream of reattachment on a hollow cylinder–flare set-up. A notable outcome was that the conical forebody reduced the prominence of these vortices. These streamwise vortices correlated with high heat flux streaks at the wall near reattachment, and potentially triggered transition to turbulence. More recent work by Dwivedi *et al.* (2019) has further clarified that base-flow deceleration substantially amplifies streamwise velocity, while baroclinic effects generate streamwise vorticity. This study also revealed that temperature streaks near reattachment arise from the amplified growth of streamwise velocity and vorticity perturbations, compounded by the enhancement of upstream temperature perturbations, through the reattachment shock.

Due to the sufficiently high edge Mach number in the present study, the HBL may also sustain Mack's second mode (Mack 1990), which has been well-documented over canonical geometries like flat plates and slender cones. However, its interactions with separated regions are still not fully characterized. For example, Adams (2001) found that, over a compression ramp, the second mode did not amplify within a laminar separation bubble, whereas Balakumar, Zhao & Atkins (2005) observed its amplification postreattachment. Similar behaviour was noted in quiet tunnel experiments by Benitez *et al.* (2020) on a CCF with a 10° flare angle, where both second mode and shear layer instabilities appeared postreattachment. In this study, sufficiently large-amplitude broadband disturbance was introduced upstream of separation, resulting in the amplification of shear layer instabilities, and formation of convecting turbulent spots downstream, without fully undergoing transition. Further work by Paredes *et al.* (2022) indicated that a slight increase in the flare angle could destabilize both shear and boundary layers sufficiently, to induce transition under low-disturbance conditions. Experiments by Benitez *et al.* (2023*a*) using a 12° flare angle in a quiet tunnel revealed an amplified shear layer mode in the frequency band of Mack's first mode in the postreattachment region, and noted the re-emergence of the second mode over the flare, despite its dampening over the cylinder. They also observed turbulent spot formation, inferred to be generated by shear layer instability wave packets. Recently, Caillaud *et al.* (2024) applied resolvent analysis to study non-modal disturbance growth across various Reynolds numbers on sharp and blunt nose-tip CCF geometries, finding substantial amplification of the first and second modes in sharp-tip cases, while both were stabilized in the blunt-nose configurations. Their analysis identified a low-frequency instability mechanism similar to the first mode in the shear layer, and a high-frequency mechanism akin to the second mode within the separation bubble, for sharp-tip geometries.

Another factor that compounds flow complexity in the presence of the above instability dynamics is their sensitivity to free stream disturbance levels. This was evidenced in recent experiments conducted by Benitez *et al.* (2024) on a blunt CCF at multiple facilities, where they observed differences in the reattachment location of the separation region, state of the boundary layer post reattachment and instabilities amplified in the flow, which were hypothesized to be caused due to differences in tunnel noise properties, among other factors. In the present case, while we expect some of the modal instabilities to define transitional pathways under low free stream perturbation amplitudes, non-modal or bypass mechanisms Morkovin (1985) may take over at sufficiently high perturbation amplitudes, circumventing the growth of primary and associated secondary modes. The penetration of low-frequency vortical disturbances into the boundary layer facilitated by high-frequency shielding phenomena (Hunt & Durbin 1999; Zaki & Durbin 2005), the resulting streak formation due to lift-up effects (Landahl 1980; Jacobs & Durbin 2001) and eventual turbulent spot generation through secondary instabilities (Andersson *et al.* 2001; Ovchinnikov, Choudhari & Piomelli 2008) could result in potential unique transition mechanisms over these hypersonic configurations. Such pathways were observed in studies by Lugrin *et al.* (2021) for a Mach 5 axisymmetric compression ramp subjected to white noise forcing. They observed that the amplification of the oblique first mode was higher than the second mode, which resulted in nonlinearly generated streaks. The nonlinear forcing associated with these streaks initiates a linear amplification mechanism driven by centrifugal, baroclinic or lift-up effects within the mixing layer and reattachment region, ultimately leading to flow breakdown.

The present work builds on the above efforts on CCF-based geometries, with the aim of understanding transition sensitivity of a typical flow field sustaining multimodal mechanisms, to free stream disturbance levels. While it is generally accepted that higher free stream disturbance amplitudes promote earlier transition onset, a comprehensive quantification of this effect is still lacking, particularly for flight relevant configurations with the above discussed flow complexities. To this end, we first evaluate the laminar flow field of the relevant CCF configuration, and perform a global stability analysis to identify the natural modes of instabilities in the flow field. Then direct numerical simulations (DNS) are performed at carefully designed free stream perturbation levels, enabling a detailed analysis of resulting transition dynamics.

Following the description of the geometry in § 2, § 3 details the numerics of the DNS and stability solvers. Section 4 presents validation of the laminar flow solutions obtained from axisymmetric simulations, using data from the published literature. Section 5 examines key flow features of the mean and instantaneous flow fields resulting from variations in free stream amplitude. Mechanisms driving boundary layer transition under different free stream conditions are explored in § 6, followed by an analysis of the ensuing aerothermal loading in § 7.

2. Geometry and flow conditions

The flow field examined in this work is informed by recent experiments on a CCF configuration conducted by Benitez *et al.* (2023*b*), in the Boeing-AFOSR Mach-6 Quiet Tunnel (BAM6QT) at Purdue University. Figure 1 presents the geometric details of the CCF model, and representative flow features around it. The CCF consists of a 5° half-angle cone and a 12° flare, with dimensions identical to those used in these experiments. The cone segment has a length of 399 mm (15.7″), and a base radius of 35 mm (1.37″). The nose of the cone is modelled as a sharp tip, since no major bluntness effects were reported in the corresponding experimental geometry, which utilized a 0.1 mm nose radius, corresponding to 0.175 % of the cone base radius. The cone–cylinder junction forms a sharp expansion corner, downstream of which the cylinder extends for a length of 147 mm (5.78″). The cylinder–flare junction forms a sharp compression corner, followed by the flare extending for a distance of 105 mm (4.13″), with its radius increasing from 35 mm (1.37″) to 57 mm (2.24″).

The flow conditions in the current study match the experimental conditions, with a free stream Mach number, $M_\infty = 6.0$, free stream velocity, $U^*_\infty = 854.10\,\text{ms}$, free stream temperature, $T^*_\infty = 50.42\,\text{K}$, and free stream density, $\rho^*_\infty = 0.04801\,\text{kg}\,\text{m}^{-3}$. All dimensional quantities are represented by $(^*)$. Based on these free stream parameters, the incoming flow has a unit Reynolds number, $Re_\infty = 12.63 \times 10^6\,\text{m}^{-1}$. The walls of the model are maintained at a constant temperature, $T^*_w = 300\,\text{K}$. All studies are performed with the model at zero angle of attack with respect to the free stream.

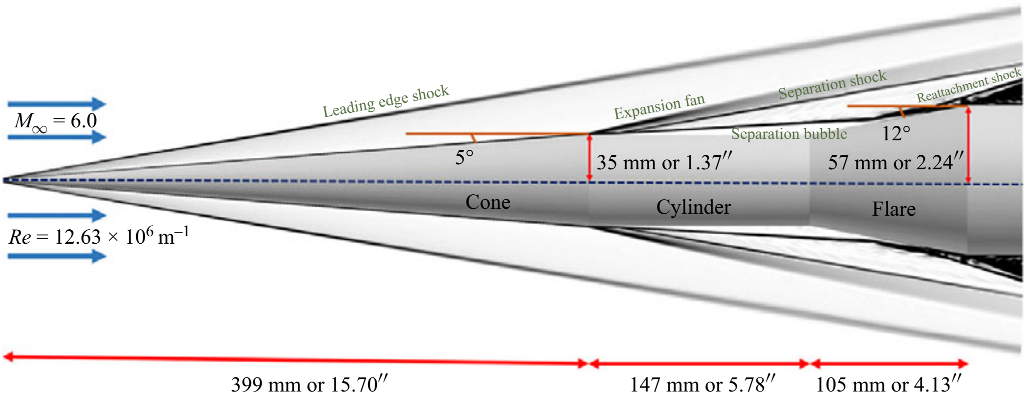

Figure 1. Geometric details of the CCF model. General flow features are shown via contours of $|\nabla\rho|$.

3. Computational framework

3.1. *Laminar simulations*

To evaluate the natural instability modes in the CCF flow field, and to initiate the DNS, it is necessary to predict its laminar basic state. This is obtained by solving the axisymmetric Navier–Stokes equations, formulated in the generalized axisymmetric coordinate system. These equations are expressed as follows:

$$\begin{aligned}\frac{\partial}{\partial\tau}\left(\frac{\boldsymbol{Q_a}}{\mathrm{J}_{\boldsymbol{a}}}\right) = -\Bigg\{&\left[\frac{\partial}{\partial\eta}\left(\hat{\boldsymbol{A}}\frac{\partial \mathrm{r}}{\partial\xi}-\hat{\boldsymbol{B}}\frac{\partial x}{\partial\xi}\right)+\frac{\partial}{\partial\xi}\left(-\hat{\boldsymbol{A}}\frac{\partial \mathrm{r}}{\partial\eta}+\hat{\boldsymbol{B}}\frac{\partial x}{\partial\eta}\right)\right]\\&+\frac{1}{\mathrm{r}}\left[\frac{\partial}{\partial\eta}\left(\hat{\boldsymbol{A}}_{\boldsymbol{r}}\frac{\partial \mathrm{r}}{\partial\xi}-\hat{\boldsymbol{B}}_{\boldsymbol{r}}\frac{\partial x}{\partial\xi}\right)+\frac{\partial}{\partial\xi}\left(-\hat{\boldsymbol{A}}_{\boldsymbol{r}}\frac{\partial \mathrm{r}}{\partial\eta}+\hat{\boldsymbol{B}}_{\boldsymbol{r}}\frac{\partial x}{\partial\eta}\right)\right]\Bigg\}\\&-\frac{1}{\mathrm{r}}\boldsymbol{D}-\frac{1}{\mathrm{r}^2}\hat{\boldsymbol{B}}_{\boldsymbol{rr}}.\end{aligned} \tag{3.1}$$

In the above, x represents the axial direction, and r represents the radial direction. The vector of conserved variables is denoted by $\boldsymbol{Q}=[\rho, \rho u, \rho v_r, \rho E]^{\mathrm{T}}$, where ρ signifies density, and (u, v_r) denotes the velocity components in the axial and radial directions, respectively. The total specific internal energy, E, is defined as $E=T/[\gamma(\gamma-1){M_\infty}^2]+(u^2+v_r^2)/2$, where T denotes the static temperature, and γ represents the ratio of specific heats. The reference Mach number is set as $M_\infty=6.0$. The Jacobian, $\mathrm{J}_a=\partial(\xi, \eta, \tau)/\partial(x, r, t)$, is employed to perform coordinate transformations from cylindrical coordinates to generalized axisymmetric coordinates. As defined in Sandberg (2007), $\hat{\boldsymbol{A}}$, $\hat{\boldsymbol{B}}$, $\boldsymbol{D}$ are combinations of inviscid and viscous fluxes, while $\hat{\boldsymbol{A}}_r$, $\hat{\boldsymbol{B}}_r$, $\hat{\boldsymbol{B}}_{rr}$ contain only the viscous fluxes.

Since the axisymmetric simulation is performed to acquire the laminar flow, spatial derivatives are discretized using a second-order central finite difference scheme, with a fourth-order diffusion term (Jameson, Schmidt & Turkel 1981; Vatsa & Wedan 1990) incorporated to mitigate numerical instabilities in the smooth regions of the flow field. Near discontinuities, numerical diffusion is adjusted to second order through a total-variation-diminishing approach for shock detection (Swanson & Turkel 1992; Vatsa 1995). Time integration is performed using a nonlinearly stable third-order Runge–Kutta scheme (Shu & Osher 1988).

The computational grid comprises of approximately 1.3×10^6 nodes, with 2987 nodes in the streamwise direction and 431 nodes in the wall-normal direction. Close to the walls, the grid is refined to achieve a minimum spacing of 1×10^{-4} in the wall-normal direction. Towards the outflow boundaries, the grid is stretched progressively to prevent numerical reflections within the domain. The near-wall region is resolved using 198 nodes within the laminar boundary layer, as evaluated prior to the separation over the cylindrical segment. Dirichlet BCs on primitive variables are utilized to impose free stream conditions at the inflow plane, while zero gradient outflow conditions are imposed at the outer and downstream outflow boundaries. The walls are treated using no-slip isothermal conditions with a constant wall temperature, $T_w \sim 5.95T_\infty$. The laminar calculations were iterated on multiple preliminary grids to ensure that the shock is sufficiently resolved in the inviscid region.

3.2. *Direct numerical simulations*

The scale-resolved simulations necessary to predict the transitional and turbulent states of the HBL developing over the CCF are performed by solving the following three-dimensional Navier–Stokes equations, cast in curvilinear coordinates,

$$\frac{\partial}{\partial \tau}\left(\frac{\boldsymbol{Q}}{J}\right) = -\left[\left(\frac{\partial \boldsymbol{F_i}}{\partial \xi} + \frac{\partial \boldsymbol{G_i}}{\partial \eta} + \frac{\partial \boldsymbol{H_i}}{\partial \zeta}\right) + \frac{1}{\mathrm{R}e}\left(\frac{\partial \boldsymbol{F_v}}{\partial \xi} + \frac{\partial \boldsymbol{G_v}}{\partial \eta} + \frac{\partial \boldsymbol{H_v}}{\partial \zeta}\right)\right]. \tag{3.2}$$

In the above, conserved variables are represented by $\boldsymbol{Q} = [\rho, \rho u, \rho v, \rho w, \rho E]^T$, where ρ denotes density, and (u, v, w) denote the velocity components in a Cartesian coordinate system. The total specific internal energy, E, is now defined as $E = T/[\gamma(\gamma - 1) {M_\infty}^2] + (u^2 + v^2 + w^2)/2$, where T represents the static temperature and γ represents the ratio of specific heats. The Jacobian of coordinate transformation is defined as $J = \partial(\xi, \eta, \zeta, \tau)/\partial(x, y, z, t)$. Inviscid fluxes are denoted as $(\boldsymbol{F_i}, \boldsymbol{G_i}, \boldsymbol{H_i})$, and viscous fluxes are $(\boldsymbol{F_v}, \boldsymbol{G_v}, \boldsymbol{H_v})$. The equation is closed using the ideal gas law, $p = \rho T/\gamma {M_\infty}^2$, with a constant Prandtl number, $Pr = 0.72$. Changes in dynamic viscosity with temperature are modelled using Sutherland's law.

All primitive variables are non-dimensionalized relative to their respective values at the free stream, except for pressure, which is non-dimensionalized using the dynamic pressure, defined as $p = p^*/(\rho^*_\infty u^{*2}_\infty)$. The base radius of the flare, $r^*_B = 57\,\mathrm{mm}$ or $2.24''$, serves as the reference length scale. The Reynolds number is then calculated as $Re = \rho^*_\infty u^*_\infty r^*_B/\mu^*_\infty \sim 719\,910$. Time is non-dimensionalized using a characteristic time scale based on the reference length and free stream velocity denoted as $T^*_C = r^*_B/u^*_\infty$ and $t = t^*/T^*_C$. A non-dimensional time step, $\Delta t^*/T^*_C = 1 \times 10^{-4}$, is employed for time integration resulting in a maximum Courant-Friedrichs-Lewy number $\leqslant 1$. The Strouhal number defines the non-dimensional frequency, and can be expressed as $St = f^* r^*_B/u^*_\infty$, where f^* is the dimensional frequency in hertz. The temporal evolution of the flow is computed for over a period of 30 characteristic times at a sampling rate corresponding to $St = 400$.

The convective fluxes are discretized using the third-order monotonic upstream-centred scheme for conservation laws (MUSCL) (Van Leer 1974) reconstruction method. Interface fluxes are computed using the Roe scheme (Roe 1981). Viscous fluxes are evaluated using the fourth-order central difference. Temporal integration is performed using the second-order diagonalized (Pulliam & Chaussee 1981) implicit beam-warming method (Beam & Warming 1978). This solver has been previously validated and applied in studies of high-speed boundary layer transition (Unnikrishnan & Gaitonde 2020; Aswathy Nair & Unnikrishnan 2024).

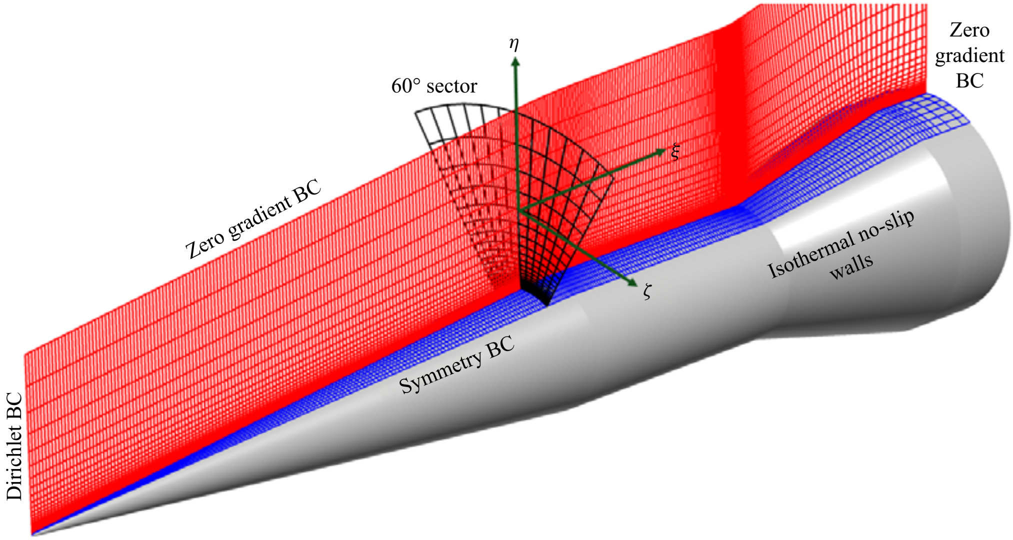

Figure 2. Computational domain and grid used for current study. Every 10th point is shown. Boundary conditions used in the simulations are also shown.

The computational domain utilized for the DNS is illustrated in figure 2. The azimuthal grid planes are identical to those used in the axisymmetric simulation described earlier. Most of the reported results are obtained from three-dimensional simulations conducted within a 60° sector of the model, discretized using 121 nodes in the azimuthal direction, resulting in a grid consisting of approximately 155×10^6 nodes. Identical to the axisymmetric solver, Dirichlet BCs are used to enforce free stream conditions at the inflow plane, and zero gradient outflow conditions are applied at the outer and downstream outflow boundaries. Symmetry BCs are imposed on the azimuthal faces of the 60° sector, while the walls are treated with no-slip isothermal conditions at a constant temperature of $T_w \sim 5.95T_\infty$. As discussed in Hader & Fasel (2019) and Hader, Deng & Fasel (2021), the use of symmetry BCs on a domain sector of angle, θ_D, results in, $k_D = 2\pi/\theta_D$, as the lowest wavenumber resolved in the computations. The azimuthal scales from the DNS are then interpreted as integer multiples of k_D.

To investigate the impact of free stream noise on transition dynamics and aerodynamic loading of the CCF geometry, spatiotemporally correlated pressure and velocity perturbations, simulated using the digital filter approach (Adler *et al.* 2018), are introduced as Dirichlet BCs on the inflow plane. Details about the free stream noise generation approach and noise characteristics are discussed in Appendix A. These perturbations cover a wide spectral range, with two different root mean square (r.m.s.) values of velocity fluctuations, including, 0.01 % (low), and 0.1 % (high), of free stream values. These two cases will be henceforth referred to as ‘DNS-L’ and ‘DNS-H’, respectively. An intermediate case of 0.05 % was also tested, but is not included here for brevity, since it showed characteristics comparable to those in DNS-H. A similar approach for imposing free stream perturbations has been demonstrated in a prior effort on transition studies over hypersonic tangent-ogive forebodies (Aswathy Nair & Unnikrishnan 2024). Since coloured perturbations are introduced at the inflow plane upstream of leading edge shock, it has the potential to excite vortical, acoustic and entropic modes in the flow. To ensure domain independency of the flow features, an additional computation of DNS-L was performed on a 90° sector of the model. No appreciable differences were observed between the 60° and 90° sectors, as demonstrated in Appendix B.

3.3. *Linear analysis framework*

A hydrodynamic instability characterization of the laminar basic state is desirable, when identifying potential transition mechanisms over the CCF. This stability analysis is performed using the Navier–Stokes-based mean flow perturbation (NS-MFP) approach. The NS-MFP approach solves the linearized form of (3.2) as detailed in Ranjan *et al.* (2020, 2021), using an implicit linearization, thus adopting a time-stepper-like approach. This is achieved by applying a body force constraint on the nonlinear Navier–Stokes equations, to obtain the linearized system summarized as follows:

$$\frac{\partial \boldsymbol{Q}'}{\partial t} = \left[\frac{\partial \boldsymbol{F}(\bar{\boldsymbol{Q}})}{\partial \bar{\boldsymbol{Q}}}\right]\boldsymbol{Q}', \quad \left[\frac{\partial \boldsymbol{F}(\bar{\boldsymbol{Q}})}{\partial \bar{\boldsymbol{Q}}}\right] = \boldsymbol{A}(\bar{\boldsymbol{Q}}). \tag{3.3}$$

In this context, $\boldsymbol{Q}'$ represents the linear perturbations in the conserved variables, $\bar{\boldsymbol{Q}}$ is the basic state chosen for the linear analysis and $\boldsymbol{A}(\bar{\boldsymbol{Q}})$ is the Jacobian representing the spatial operations in the linearized operator. The basic state, $\bar{Q}$, is obtained from the converged laminar simulation. To perform the fully three-dimensional stability analysis, the laminar flow field is then rotated 360° about the centreline axis. The computational grid for linear analysis contains half the number of points in the streamwise and wall-normal directions compared with those used in the DNS and laminar simulations, along with 360 points in the azimuthal direction. The spatial discretization schemes in NS-MFP are identical to those used in the previously described DNS, while temporal integration is performed using a third-order explicit Runge–Kutta scheme.

A Dirichlet condition on fluctuating pressure is utilized to introduce linearly constrained perturbations in NS-MFP. Specific details of this forcing will be provided in the context of various stability studies reported in the following sections. In general, perturbations are introduced at low amplitudes to ensure linearity. A non-dimensional time step size, $\Delta t = 1 \times 10^{-3}$, is employed to temporally advance the linear perturbations, and its statistics are obtained for 10 characteristic times at a sampling rate, $St = 50$.

4. Validation

The laminar baseflow obtained through axisymmetric simulations is depicted in figure 3 using Mach number contours. This laminar flow field is also validated against digitized data from computations conducted by Caillaud *et al.* (2024) under identical flow conditions and geometry. Velocity and temperature profiles at the cylinder–flare junction are compared between the two simulations in figures 4(*a*) and 4(*b*), respectively. These profiles are plotted against the height off the surface (d_n), normal to the wall along the black dashed line shown in figure 3. Additionally, the pressure variation along the wall of the CCF geometry is compared in figure 4(*c*). These comparisons reveal general agreement between the current simulations and the reference computations. The velocity drop in the profiles are indicative of boundary layer separation, and predict elevated temperatures below the shear layer. The peak reverse velocity and peak temperature within the boundary layer show reasonable comparison with the reference computations, while some mismatch exists in the near wall region, which might be attributed to errors from digitizing the profiles. The positions where the boundary layer separates and reattaches as characterized by inflections in pressure are in reasonable agreement. The pressure distribution over the flare shows a mismatch where the current computations predict a steeper pressure rise than the reference data. This may be attributed to the resolution of the reattachment shock over the flare. It has to be noted that the present trends were also consistently reproduced by both the laminar solver and the DNS solver, as will be evident in the following sections.

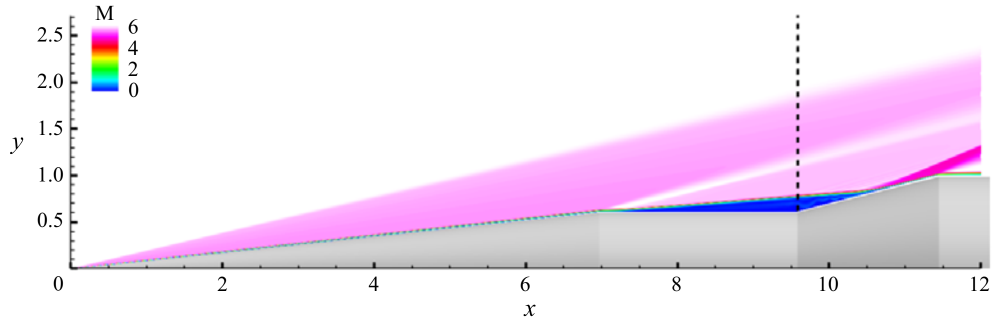

Figure 3. Laminar flow field obtained from axisymmetric simulations shown using contours of Mach number. Profiles for validation are obtained along the black dashed line. Figure is not to scale.

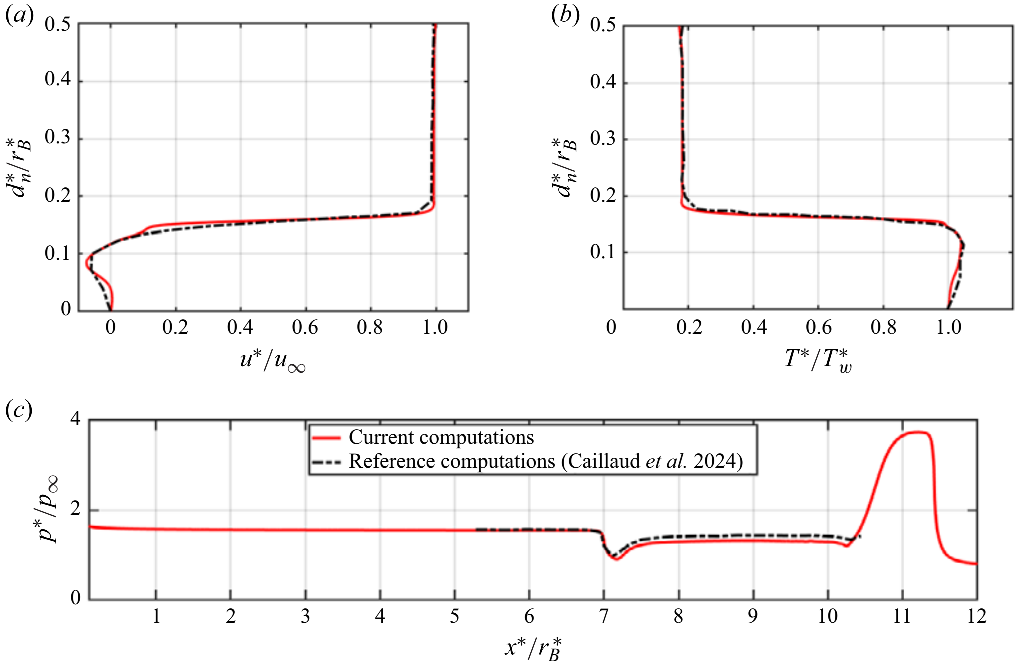

Figure 4. (*a*) Streamwise velocity, (*b*) temperature and (*c*) wall pressure comparison between current computations and computations by Caillaud *et al.* (2024). The chosen axial position has been marked by the dashed black line in figure 3.

5. Inflow effects on flow development

In flow fields sustaining multimodal mechanisms, the inflow perturbation environment has a significant impact on the realized flow field. Therefore, we first provide a systematic comparison of overall flow features observed in the two cases (DNS-L and DNS-H) in this section, along with the laminar basic state as a benchmark.

Figure 5 compares the flow features of the laminar flow field with the time averaged flow field obtained from the low-amplitude and high-amplitude DNSs, DNS-L and DNS-H, respectively. These are shown via contours of density gradient magnitude, $|\nabla \rho|$, on the midazimuthal plane of the DNS domain (earlier shown in figure 2). Major flow features identifiable in these contours are marked with numerals I–VII. Inviscid flow

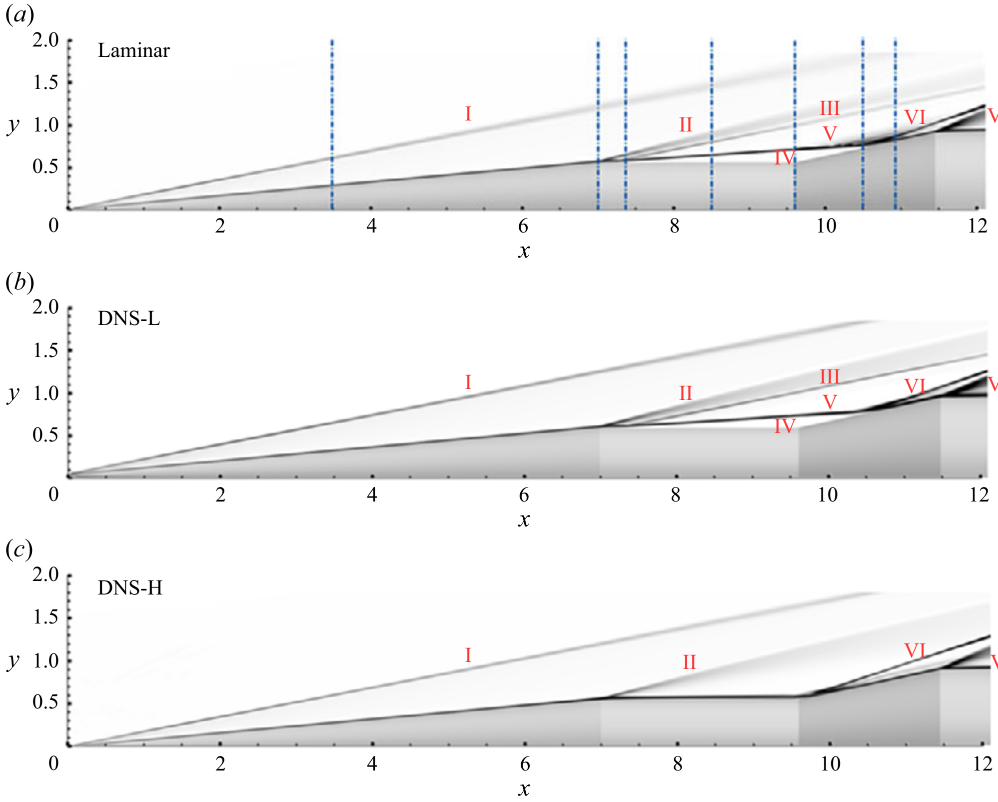

Figure 5. Comparison of flow features for (*a*) laminar, (*b*) DNS-L and (*c*) DNS-H shown via 100 equally spaced contours of $|\nabla \rho|$ between 0 and 10. Major flow features are marked with numerals I–VII. The blue dashed–dot vertical lines indicate locations where velocity profiles are extracted for comparison.

features appearing across the three cases include the conical shock produced by the sharp nose of the cone (denoted as I), an expansion fan (denoted as II) at the cone–cylinder junction ($x = 7$) and an expansion fan (denoted as VII) downstream of the flare region ($x = 11$).

The laminar flow field (figure 5*a*) and DNS-L (figure 5*b*) exhibit several additional flow features, compared with DNS-H (figure 5*c*). The most significant is a separation bubble (denoted as IV), with its separation point located slightly downstream of the expansion corner, and the reattachment point situated approximately midway along the flare. Additionally, a separation shock (denoted as III) appears at the separation point of the boundary layer. The flow above the separation bubble is characterized by a shear layer (denoted as V), and the associated compression waves and a reattachment shock (denoted as VI) near the reattachment point. The separation bubble in the laminar flow field suggests the presence of a strong adverse pressure gradient, causing the flow to detach. Retention of this separation region in DNS-L, in contrast to a nearly fully attached boundary layer over the cylinder and flare in DNS-H, highlights the differences in the states of the boundary layer, depending on inflow perturbation amplitudes. Enhanced tendency to separate in DNS-L suggests that the boundary layer is mostly laminar downstream of the expansion corner at $x = 7$, while it has attained a transitional state in DNS-H, making it less prone to separation.

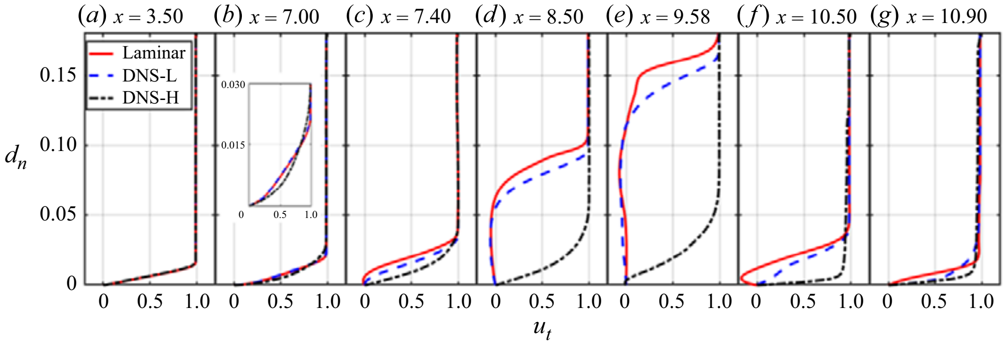

Figure 6. Variation of wall tangential velocity with height off the wall at various streamwise locations marked by the blue dashed–dot lines in figure 5. Inset figure in (*b*) shows a magnified view of the near wall profiles.

These features are further detailed in figure 6, which shows the variation of wall-tangential velocity with height off the wall at various streamwise locations marked by the blue dashed–dot (u_t) lines in figure 5. These (d_n) locations are chosen to provide a holistic understanding of the flow field over the CCF geometry. Here $x = 3.50$ is midway over the cone, where the state of the boundary layer is mostly laminar for both DNS-L and DNS-H. Deviation from laminar flow is observed in DNS-H at $x = 7.00$, which is the location of the expansion corner at the cone–cylinder junction. Here, DNS-H exhibits a fuller velocity profile, indicating the onset of transition upstream of this location. In contrast, DNS-L has a profile identical to that of the laminar solution. Presence of negative velocities indicate the first appearance of separation and flow reversal at $x = 7.40$ in the laminar flow field, while DNS-L is observed to tend towards flow reversal. As shown at $x = 8.50$, the region of negative velocity spans a larger wall normal extent in the laminar flow field when compared with DNS-L, suggesting that the size of the separation bubble is larger in the laminar solution. As a consequence, the shear layer spreading rate is expected to be higher in DNS-L compared with the laminar flow field, consistent with a state change of shear layer from laminar to transitional (Ho & Huerre 1984). At $x = 7.40$ and $x = 8.50$, DNS-H shows an attached boundary layer.

At the compression corner formed by the cylinder–flare junction ($x = 9.58$), presence of a steep adverse pressure gradient elevates the size of the separation bubble in both DNS-L and laminar flow field, exaggerating their size disparities. Having already achieved a nearly turbulized state, DNS-H is more resilient to separation, thus minimizing the region of negative velocity and resulting in a minuscule separation zone at the compression corner. At $x = 10.50$, DNS-L displays a reattached profile, while the velocity profile of the laminar solution indicates significant flow reversal closer to the wall. Thus, the height and length of the separation bubble is smaller in DNS-L, compared with the fully laminar flow field. Here DNS-H shows a much fuller velocity profile with large wall-normal gradients, indicative of a nearly fully turbulent flow. Towards the end of the flare ($x = 10.90$), the DNS-L flow field is still observed to be in the transitional regime, as evidenced by its intermediate profile flanked by the fully turbulent DNS-H profile and the laminar profile.

To quantify the turbulized state of the boundary layer in DNS-H on the surface of the flare, the velocity profile at $x = 10.50$ is plotted in wall units (u_t^+, d_n^+) in figure 7(*a*). Here, $u_t^+ = u_t/u_\tau$, and $d_n^+ = d_n u_\tau/\nu$, where $u_\tau = \sqrt{\tau_w/\rho}$, and $\tau_w = \mu_w((\partial u_t)/(\partial d_n))_{d_n=0}$. To account for compressibility effects, the van Driest transformation (Van Driest 1951) is applied to obtain the transformed velocity profiles. A viscous sublayer is observed until $d_n^+ \sim 10$, where, the relationship $u_t^+ = d_n^+$ is followed. A good match with the log-law is

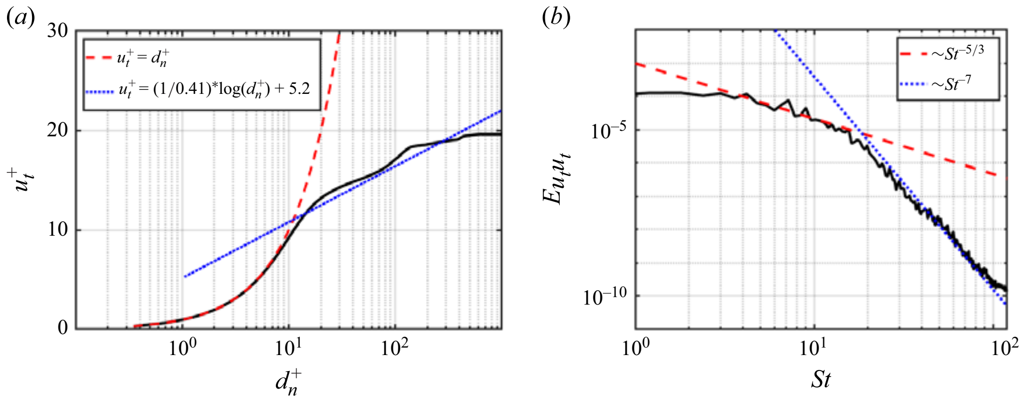

Figure 7. (*a*) Tangential velocity profile of DNS-H at $x = 10.50$ plotted in wall units. Reference curves for the viscous sublayer and log-layer are also included. (*b*) One-dimensional energy spectra calculated from wall tangential velocity fluctuations at $x = 10.5$. $St^{-5/3}$ and St^{-7} lines are also indicated.

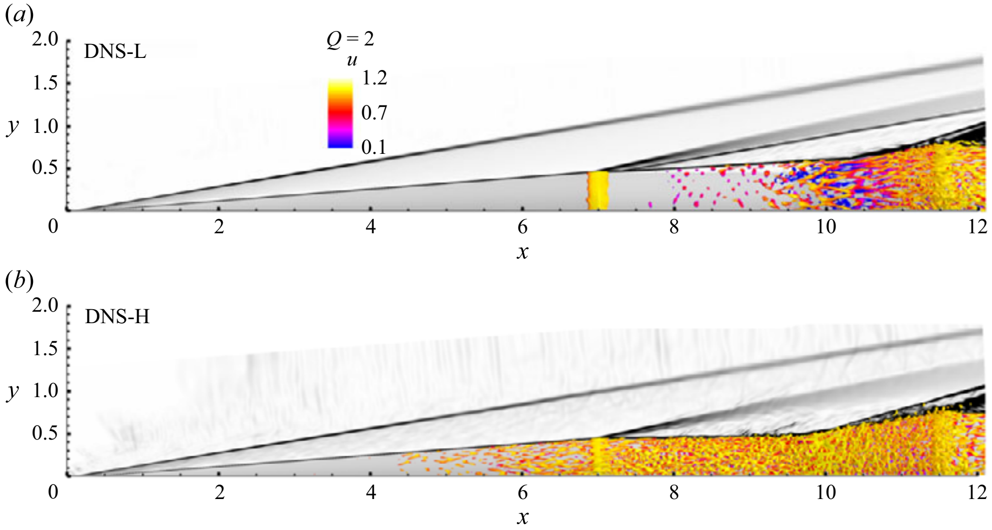

Figure 8. Comparison of instantaneous flow features for (*a*) DNS-L and (*b*) DNS-H shown via 100 equally spaced contours of $|\nabla\rho|$ between 0 and 10. Vortical structures in the flow are shown via isolevels of Q-criterion $= 2$, coloured by streamwise velocity.

also observed at $d_n^+ > 20$, consistent with a fully developed turbulent boundary layer at this location. To characterize the associated fluctuations in the boundary layer, a one-dimensional energy spectrum is constructed and presented in figure 7(*b*). The energy spectrum reveals a well-developed inertial sub range characterized by a power–law scaling of $St^{-5/3}$, followed by a dissipation range exhibiting a St^{-7} roll-off. These characteristics reaffirm that a fully turbulent boundary layer is established downstream of the compression corner in DNS-H.

The above flow features can also be observed distinctively from an instantaneous flow field shown in figures 8(*a*) and 8(*b*), for DNS-L and DNS-H, respectively, using contours of $|\nabla\rho|$. Vortical structures within the flow are highlighted via isolevels of Q-criterion, coloured by streamwise velocity. In DNS-L, the flow exhibits a predominantly laminar boundary layer over the cone, with amplification of shear layer instabilities over the separation region, and signs of transition becoming evident near the reattachment zone. This is marked by the formation of hairpin vortices and streamwise streaks downstream of the reattachment point, indicating breakdown and the onset of turbulence in this region. In comparison, an upstream shift of the transition onset location is evident in DNS-H, along with a fully turbulent flow over the flare. These mechanisms and the associated boundary layer structures will be evaluated in detail in the following section.

6. Transition mechanisms

Observations from the previous section indicate that free stream perturbation amplitude plays a significant role in altering the flow features by affecting the spatial location and mechanism of transition. Therefore, we provide a detailed analysis of relevant instabilities and their interactions that determine specific transition pathways in low and high amplitude perturbation environments, over this CCF geometry.

6.1. *Low free stream perturbation amplitude environment*

Similarities between DNS-L and the laminar solution in terms of flow features and state of the boundary layer until reattachment suggest that a modal route of transition (e.g. path A suggested by Morkovin 1994) is likely in this case. This is best studied by first identifying the underlying instabilities of the laminar basic state, which is now reported through a global linear analysis. We evaluate the linear perturbation spectra and relevant instability eigenfunctions of the laminar solution using the NS-MFP technique, earlier introduced in § 3.3.

6.1.1. *Linear analysis of the laminar basic state*

In the current approach, the laminar basic state is linearly forced in a continuous manner, by introducing random perturbations in pressure at the inflow plane. A forcing amplitude study was also performed to ensure linearity. Figure 9(*a*) shows the wall pressure spectra of these linearly constrained fluctuations. The broadband spectra near the inflow are characteristic of the random nature of the imposed inflow perturbations, which is persistent until $x \sim 2.5$. The growing boundary layer over the cone behaves as a low-pass filter to the incoming perturbations (Ovchinnikov *et al.* 2008), selectively amplifying lower frequencies ($20 \leqslant f^* \leqslant 50\,\text{kHz}$), marked by the blue rectangle in figure 9(*a*). These frequencies are in the realm of Mack's first mode instability Mack (1984).

Downstream of the expansion corner at $x = 7$, multiple bands (marked by the red circle in figure 9*a*) appear due to the amplification of shear layer instabilities. As the boundary layer separates and forms a separation bubble, a shear layer develops above it, growing and spreading by entraining ambient fluid. This results in the characteristic $1/x$-type variation of the spectral signature. The primary mechanism driving shear layer perturbation amplification is the Kelvin–Helmholtz (K-H) instability (Helmholtz 1868; Thomson 1871). The highest amplification rates for K-H instabilities in shear layers typically occur around a frequency, $St_\theta = f^*\theta^*/u^*_\infty \sim 0.012{-}0.017$, where, θ^* is the momentum thickness of the upstream boundary layer prior to separation. In the current case, the momentum thickness is found to be $\theta^* = 0.0684$ mm, leading to $St_\theta = 0.01$ for $f^* \sim 128\,\text{kHz}$ seen at $x \sim 7.4$. This matches very well with the band of frequencies at which the shear layer instabilities were observed in the experiments by Benitez *et al.* (2023*b*). These frequencies also align closely with observations in other shear layers and mixing layers (Michalke 1965; Gutmark & Ho 1983; Hussain 1986; Lakshmi Narasimha Prasad & Unnikrishnan 2024).

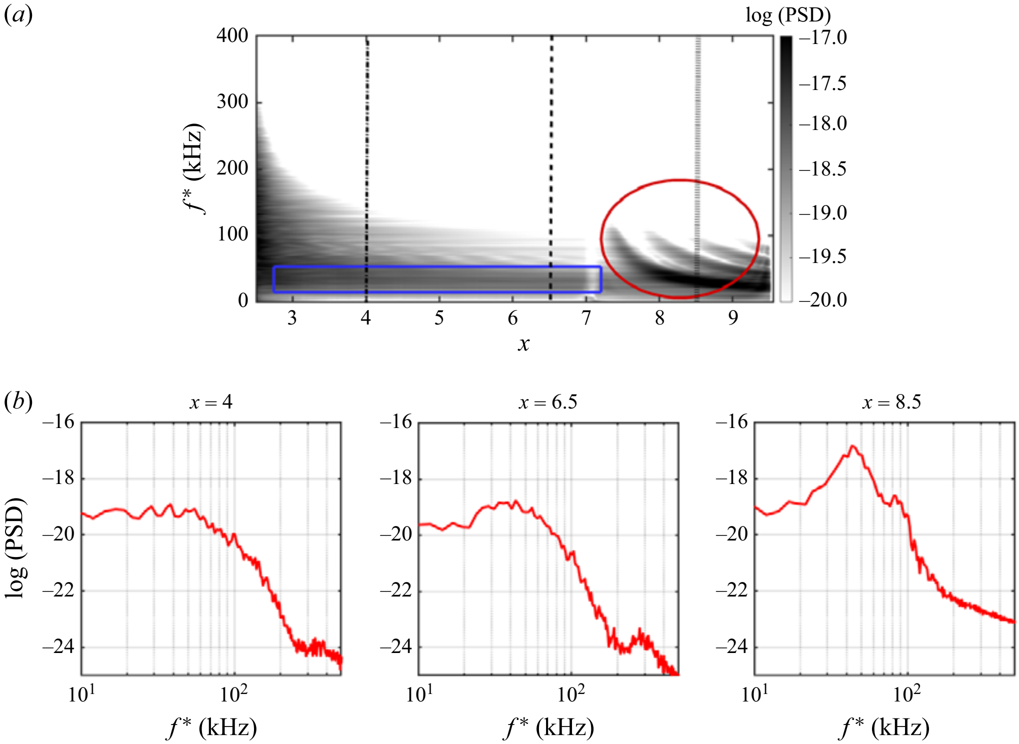

Figure 9. (*a*) Streamwise variation of linear wall pressure spectra. The blue rectangle and the red circle mark signatures of first mode and shear layer modes, respectively. (*b*) Power spectra plots at $x = 4$, 6.5 and 8.5 (black dash–dot, dash and dotted lines, respectively, in panel (*a*)).

The linear spectra are further quantified in figure 9(*b*) using the logarithm of power spectra at three streamwise locations, $x = 4$, 6.5 and 8.5, as marked by the black dash–dot, dashed and dotted lines, respectively, in figure 9(*a*). The spectrum at $x = 4$ is dominated by low frequencies in the realm of first mode, with $f^* \leqslant 50$ kHz. At $x = 6.5$, in addition to the dominant first mode broadband peak at $f^* \sim 35$ kHz, a high frequency peak centred around $f^* \sim 272$ kHz is visible. This frequency corresponds to Mack's second mode instability (Mack 1990). The corresponding second mode frequency observed in experiments by Benitez *et al.* (2023*b*) is ∼230 kHz, indicating a difference of ∼16 % from the current computational predictions. It has to be noted that the current linear spectrum identifies the second mode waves to be of relatively lower amplitudes than the first mode waves, primarily due to the three-dimensional nature of the forcing. An axisymmetry constrained linear spectrum was also evaluated to ensure that it recovers the high-frequency second modes as the dominant two-dimensional instability response of the cone boundary layer. At $x = 8.5$, characteristics of the shear layer K-H instabilities are evident with a dominant low-frequency peak at $f^* \sim 45$ kHz, and a subdominant high-frequency peak at $f^* \sim 85$ kHz.

The range of first-mode and second-mode frequencies over the cone, and the shear layer modes identified above are characteristic convective instabilities of attached and separated flows, respectively. However, the dominant separation bubble over the flare in this CCF also presents the potential of harbouring absolute instabilities. Paredes *et al.* (2022) observed this possibility in cases where the flare angle exceeds 8°. While the above-described continuous forcing is suitable to evaluate such instabilities as well,

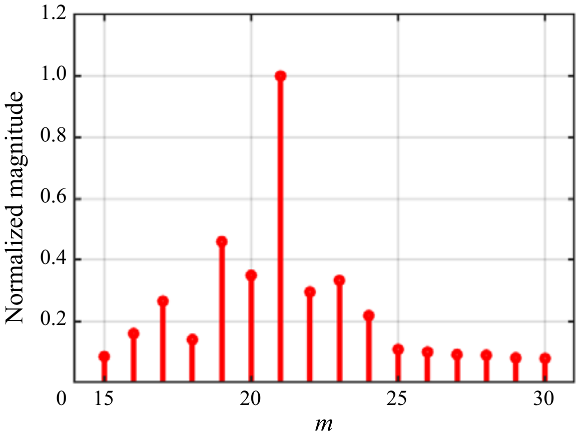

Figure 10. Wavenumber distribution of instability amplitude within the separation region.

a more rigorous approach to identify an absolute instability is a pulsed forcing approach, which helps us to evaluate the long-term perturbation dynamics of the basic state, without temporally sustained forcing. To this end, random pressure perturbations are now introduced at the domain inflow as a very short duration pulse, with $\Delta t_P = 0.05$, and are allowed to linearly evolve about the laminar basic state. Here Δt_P is the temporal window over which the random forcing is active in this pulsed excitation case. The spatial and spectral characteristics of the ensuing linear response are detailed below.

The azimuthal structure of the linear response is first quantified in the following manner, to identify the most dominant instability wavenumber in the circumferential direction:

$$q(x, r, \phi, t) = q_a^0(x, r, t) + \sum_{m=1}^{\infty} [q_a^m(x, r, t)\cos(m\phi) + q_b^m(x, r, t)\sin(m\phi)] \quad (6.1)$$

where, m refers to the azimuthal mode number and $q_a^m(x, r, t)$ and $q_b^m(x, r, t)$ are the azimuthally invariant spatial supports determined by

$$q_a^0(x, r, t) = \frac{1}{2\pi}\int_{-\pi}^{\pi} q(x, r, \phi, t)\, \mathrm{d}\phi, \quad (6.2)$$

$$q_a^m(x, r, t) = \frac{1}{\pi}\int_{-\pi}^{\pi} q(x, r, \phi, t)\cos(m\phi)\, \mathrm{d}\phi, \quad (6.3)$$

$$q_b^m(x, r, t) = \frac{1}{\pi}\int_{-\pi}^{\pi} q(x, r, \phi, t)\sin(m\phi)\, \mathrm{d}\phi. \quad (6.4)$$

The magnitude of the spatial supports, $||q|| = \sqrt{(q_a^m)^2 + (q_b^m)^2}$, is temporally averaged and then integrated in the streamwise and wall normal directions spanning $9.58 \leqslant x \leqslant 11.5$ and $0 \leqslant d_n \leqslant 0.2$, respectively, to estimate the dominant modes within the potential zone of absolute instability. A plot of normalized magnitudes for various azimuthal wavenumbers is shown in figure 10. It reveals that the instability within the separation bubble has appreciable contributions from a series of wavenumbers, including, $15 \leqslant m \leqslant 25$. However, the highest contribution is from $m = 21$, which aligns with the observations by Paredes *et al.* (2022), where, global stability analysis on a 12° flare angle predicted $m \sim 25$ to be the most amplified instability.

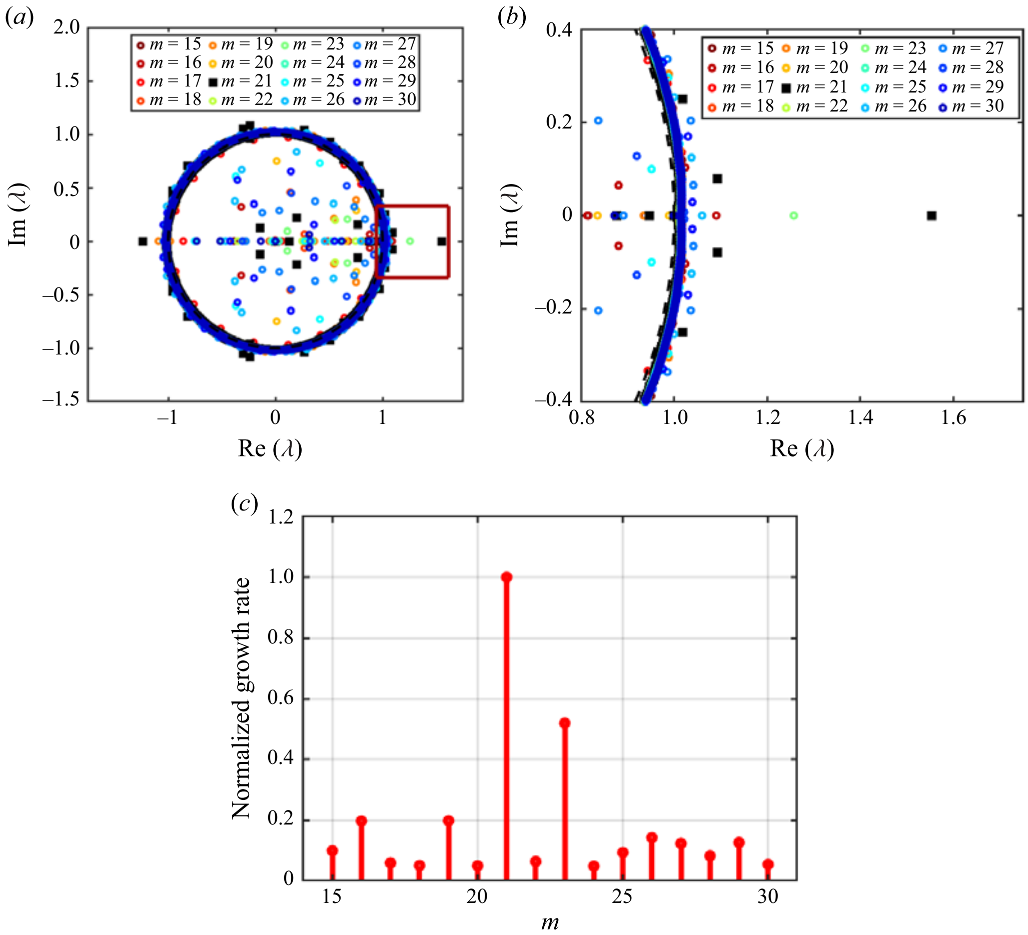

Figure 11. (*a*) Instability eigenvalue distribution about a unit circle (marked by black dashed line). (*b*) Zoomed region marked by the red box in (*a*). (*c*) Normalized growth rate of zero frequency mode for various azimuthal wavenumbers.

To estimate the instability eigenspectra and the corresponding eigenfunctions from NS-MFP, we follow the procedure in Ranjan *et al.* (2020, 2021), by performing a dynamic mode decomposition (Schmid 2010; Tu 2013) on the linearized temporal snapshots. The resulting distribution of eigenvalues about the unit circle is presented in figure 11(*a*). A portion of this spectrum with positive real component (which corresponds to its temporal growth rate) is also marked by a red box and magnified in figure 11(*b*). From the distribution in figure 11(*b*), it is evident that certain eigenvalues with zero imaginary components have significantly large temporal growth rates, that fall outside the unit circle. This indicates the presence of non-oscillating, monotonically growing instabilities in the domain. Such a presence of growing modes in the absence of an imposed perturbation is characteristic of an absolute instability in the system, in line with predictions made by Paredes *et al.* (2022). It is also evident from this distribution that $m = 21$ (black squares) has the highest growth rate, consistent with the perturbation magnitude analysis presented earlier in figure 10. This is further clarified in figure 11(*c*), which shows the distribution of normalized growth rate at zero frequency for various azimuthal wavenumbers.

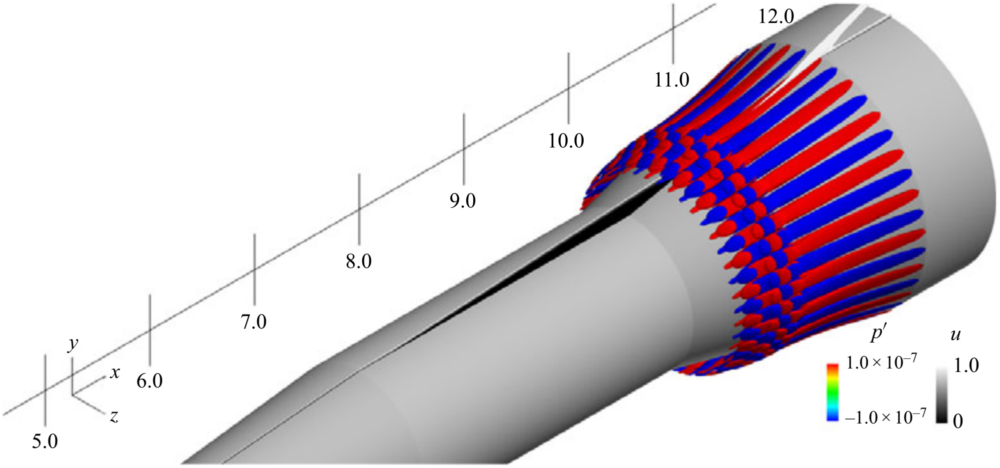

Figure 12. Spatial mode at zero frequency for $m = 21$ shown via isosurfaces of pressure fluctuations. Also included are contours of laminar streamwise velocity to highlight the separation bubble.

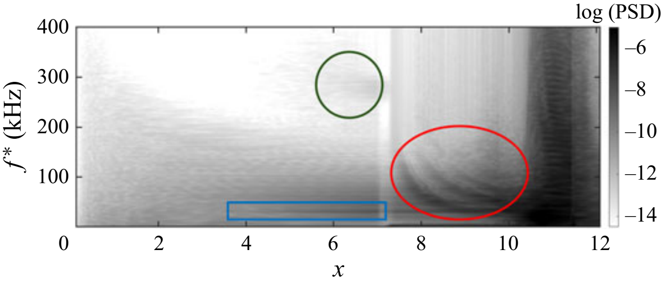

Figure 13. Streamwise variation of wall pressure spectra in DNS-L. The blue rectangle demarcates an energetic band in the regime of Mack's first mode. The green circle demarcates the energetic band corresponding to Mack's second mode. The red oval highlights the shear layer bands.

The flow field is thus seen to aggressively amplify $m = 21$, making it the most preferred wavenumber in this region, with the highest growth rate and amplitude.

The spatial form of the instability eigenfunction corresponding to the most amplified mode (zero frequency and $m = 21$) is shown in figure 12 via isosurfaces of pressure fluctuations. Laminar streamwise velocity contours are also shown to highlight the size of the separation bubble, and as a reference to interpret the location of the eigenmode. The spatial support of this eigenmode indicates the presence of streamwise streaks that originate in the shear layer, immediately downstream of the compression corner at the cylinder–flare junction. They continue to exist post reattachment of the separation region, and appear as streaks on the surface of the flare as well. This behaviour is similar to that observed in compression corners in a double wedge by Sidharth *et al.* (2018), Dwivedi *et al.* (2019) and in a CCF by Caillaud *et al.* (2024). In the context of these linear instabilities over the CCF, we now examine the transition pathways in the low-amplitude perturbation environment, as captured in DNS-L.

6.1.2. *Transition mechanism in DNS-L*

The streamwise wall pressure spectra from DNS-L is reported in figure 13, as obtained from the midplane of the DNS computational domain. Notable similarities are evident

Number of snapshots	Sampling frequency (*St*)	Window	Overlap	Number of blocks (n_{blk})	Number of frequencies (n_{fft})
2000	200	1000	50 %	3	501

Table 1. Parameters used for SPOD.

between this DNS spectra and the linear spectra of the laminar basic state (figure 9). For example, the spectral signatures of the shear layer modes range from approximately $f^* \sim 130$ kHz at $x = 7.2$, to $f^* \sim 30$ kHz at $x = 9.5$. Two distinct energetic bands are also observed over the cone, as highlighted by a green circle and a blue rectangle in figure 13. The former, centred around $f^* \sim 272$ kHz, contains relatively less energy, and emerges towards the end of the conical region. This mode, also observed in the linear analysis, corresponds to Mack's second-mode instability, and falls within the range of second-mode frequencies reported in the experiments by Benitez *et al.* (2023*a*). The energetic band marked by the blue rectangle, arising from Mack's first-mode at a lower frequency ($f^* \sim 30$ kHz), displays more energy content. This band emerges around $x \sim 4$ on the cone, and persists over a large streamwise extent, encompassing flow separation and the reattachment point. Beyond $x = 10.5$, the predominantly broadband spectral characteristics indicate the transitional nature of the flow, after reattachment on the flare. The similarities between the nonlinear (figure 13) and linear (figure 9) spectra until the reattachment point over the flare, suggests the central role of the absolute instability of the bubble in driving transition and nonlinear breakdown, in the low-amplitude perturbation environment. This inference is also supported by the similarities between the laminar and mean DNS-L flow fields, earlier discussed in figure 5.

To quantitatively extract the spatial structure of the boundary layer instabilities identified in the DNS-L pressure spectra, we employ spectral proper orthogonal decomposition (SPOD) (Towne, Schmidt & Colonius 2018; Schmidt & Colonius 2020). Due to the highly oblique nature of first-mode instabilities, it is essential to conduct the modal analysis over a three-dimensional domain to account for azimuthal variations (Lugrin *et al.* 2021). Therefore, SPOD of pressure fluctuations is performed on a subdomain of interest, spanning $4 \leqslant x \leqslant 11$ in the streamwise direction, $d_n = 0.25$ units extending from the surface in the wall-normal direction, and covering the entire azimuthal sector used in DNS-L. The parameters used for SPOD analysis are provided in table 1.

Figure 14 presents the dominant SPOD modes of pressure fluctuations at the two key frequencies previously identified in the wall pressure spectra of DNS-L (figure 13): $f^* = 32$ kHz (figure 14*a*) and $f^* = 272$ kHz (figure 14*b*). To visualize these modes, isolevels of pressure fluctuations are displayed, and the modes are symmetrically mirrored to envelop the entire geometry. For better clarity and interpretation of these modes, mean flow features are overlaid, represented by contours of $|\nabla \rho|$. The mode at $f^* = 32$ kHz begins to amplify around $x \sim 4$, exhibiting an azimuthally oblique structure characteristic of first mode instabilities. These oblique features persist across the expansion fan, and experience further amplification through the entire extent of the shear layer, until reattachment. This modal support indicates that the shear layer over the cylinder–flare separation bubble is receptive to first mode instabilities over the cone boundary layer, consistent with observations of Paredes *et al.* (2022).

In contrast, the high-frequency mode at $f^* = 272$ kHz starts to amplify near the end of the cone segment, at $x \sim 6$. These high-wavenumber structures display minimal azimuthal variation, indicative of two-dimensional planar behaviour – typical of Mack's

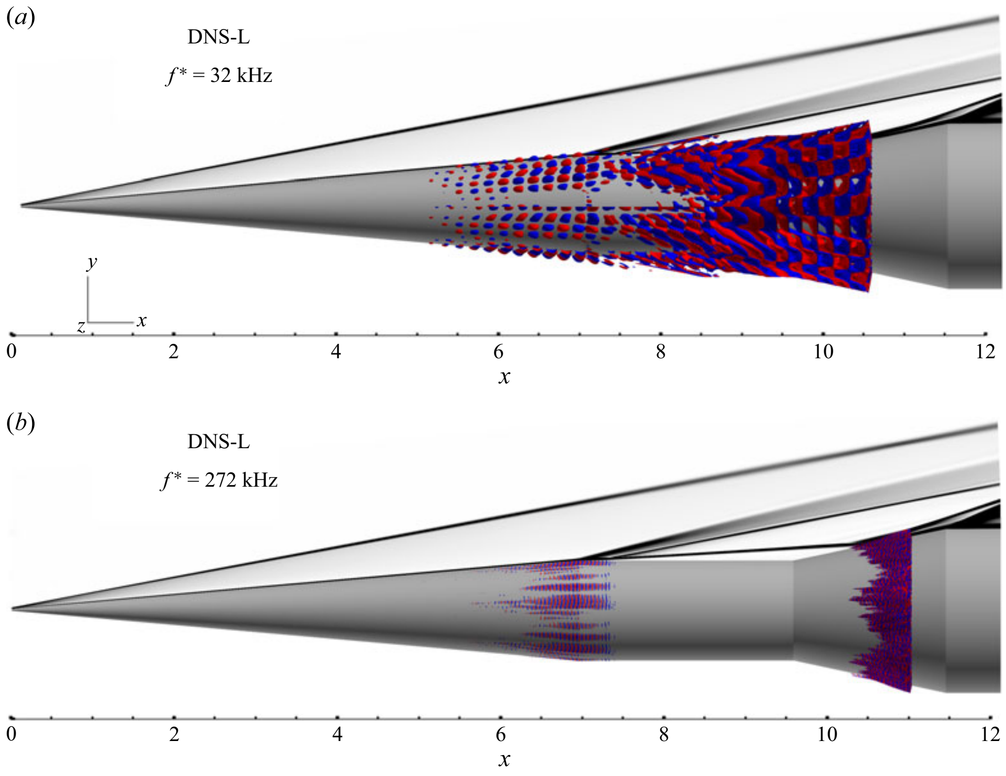

Figure 14. Dominant SPOD mode of pressure fluctuations at two frequencies: (*a*) $f^* = 32$ kHz and (*b*) $f^* = 272$ kHz corresponding to Mack's first and second modes, respectively, obtained from DNS-L. Isolevels of pressure fluctuations $= \pm 0.2$ are used to visualize the modes. Mean flow features are shown via 100 equally spaced contours of $|\nabla \rho|$ between 0 and 10.

second mode instability. While this instability sustains across the expansion waves, it does not amplify over the separation bubble. This is due to the absence of a locally supersonic boundary layer zone, which is necessary for sustaining trapped acoustic waves, a characteristic property of the second mode. Traces of this frequency are visible after reattachment in figure 14(*b*), where the flow is transitional, and may be contributed by the nearly broadband spectra seen earlier in figure 13. The quiet tunnel experiments by Benitez *et al.* (2023*b*) have also identified the second mode to amplify post reattachment, while it was neutrally stable over the separation bubble.

By combining the information from DNS-L spectra (figure 13) and the absolute instability predicted by the linear analysis (figure 12), we hypothesized earlier that these instability streaks drive transition in the low-amplitude perturbation environment. To further confirm this, we compare the wall-imprint of this linear instability, with its manifestation in DNS-L. These instability streaks result in localized increase in heat transfer and skin friction, and are therefore suitable markers for comparison. Figure 15 compares the azimuthal variation of normalized wall heat transfer coefficient, C_h (defined later in § 7), at $x = 10.5$, obtained from DNS-L, with that obtained from the linear analysis, where the $m = 21$ azimuthal mode (as shown in figure 12) dominates. Two arbitrary instantaneous realizations from DNS-L are included, since the exact azimuthal locations of these streaks vary intermittently in the nonlinear simulation. The 90° sector DNS-L is utilized for the comparison, to minimize any influence from the finite sector calculations.

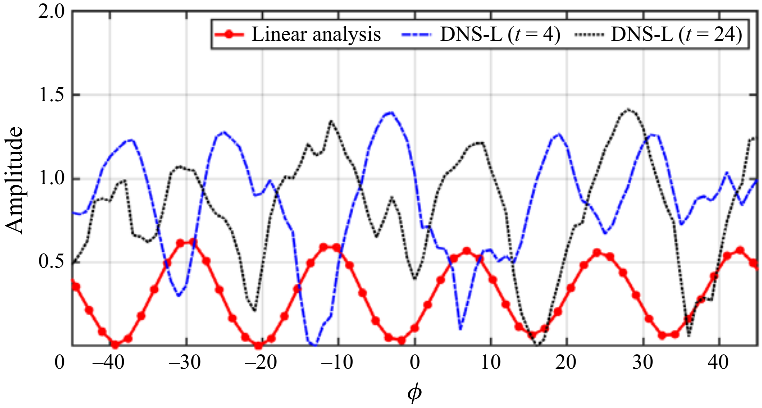

Figure 15. Comparison of azimuthal variation of normalized C_h as obtained from DNS-L at two arbitrary time instances with that obtained the linear analysis, at $x = 10.5$.

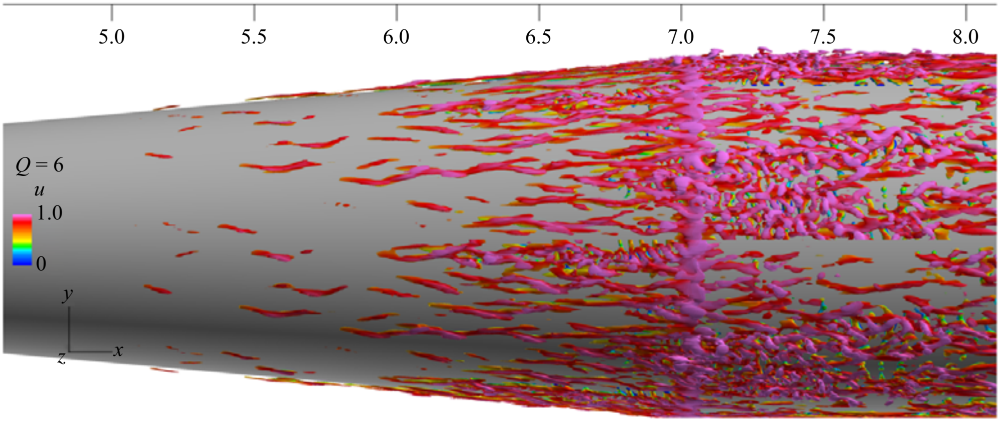

Figure 16. Instantaneous snapshot of DNS-H flow field. Vortical structures are shown via isolevel of Q-criterion = 6, coloured by streamwise velocity.

Around five prominent peaks are evident in DNS-L results, indicating the presence of an $m = 20$ mode. This matches very well with the azimuthal wavelength in the linear predictions. It suggests that the streaks in C_h observed in DNS are indeed a manifestation of the absolute instability sustained by the separated flow at the compression corner. Therefore, despite the presence of convective instabilities in the boundary and shear layers, the absolute instability of the separation bubble dominates transition in the low-amplitude perturbation environment for this CCF. In such scenarios where the transitional nature appears downstream of the reattachment point, boundary layer breakdown is often initiated by the secondary instabilities of the nonlinearly saturated streaks (Mandal, Venkatakrishnan & Dey 2010; Hack & Zaki 2014; Lugrin *et al.* 2021).

6.2. *High free stream perturbation amplitude environment*

As discussed earlier in § 5, the onset of transition shifts upstream with increase in free stream perturbation amplitude. This is evident in figure 16, which shows an instantaneous snapshot of the DNS-H flow field near the cone–cylinder junction. Vortical structures in this flow field are highlighted using Q-criterion, coloured by streamwise velocity. The

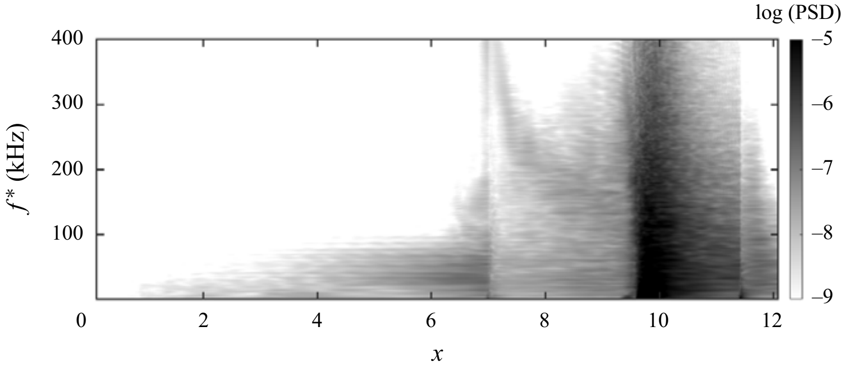

Figure 17. Streamwise variation of wall pressure spectra obtained from DNS-H.

region over the cone is dominated by streamwise streaks resembling Klebanoff modes (Matsubara & Alfredsson 2001; Wu & Choudhari 2001; Fasel 2002). As mentioned earlier in § 1, these streaks are a characteristic of bypass transition, which are often initiated by the penetration of low-frequency components of free stream turbulence into the boundary layer, facilitated by shear sheltering, where they interact with the mean flow and are amplified by the shear in the boundary layer, forming elongated streaky structures. While streaks observed near wall are generally characterized by regions of high streamwise velocity, those away from the wall correspond to low-speed streaks. Those streaks lifted away from the wall are typically more susceptible to amplifying secondary instabilities (Andersson, Berggren & Henningson 1999) in the flow, forming turbulent spots that rapidly grow in the azimuthal direction, resulting in breakdown. Further, as elucidated by Hack & Zaki (2014), the region of overlap between high- and low-speed streaks can also give rise to a near-wall secondary instability.

A quantitative analysis of this flow field is presented using its wall pressure spectra in figure 17. Towards the downstream portion of the cone segment ($x \sim 7$), energetic fluctuations in the low frequency regime ($20 \leqslant f^* \leqslant 50$ kHz) correspond to the first mode type of instabilities. In addition, the emergence of high frequency (300−400 kHz) content corresponding to the second mode can also be observed prior to the expansion corner. Contrary to DNS-L, these high frequencies are sustained downstream of the expansion zone, with their peak frequency decreasing as the boundary layer grows over the cylindrical segment. These correspond to spanwise-invariant near-wall structures with peak dilation, which have been previously observed in post-transitional HBLs (Unnikrishnan & Gaitonde 2021). The fully turbulent nature of the boundary layer is reflected in the broadband spectra at $x \sim 10$, with peak amplitudes corresponding to the location where the flare-induced shock interacts with the turbulized boundary layer, as shown earlier in figure 8.

Due to the intermittent nature of transition in DNS-H, it is illuminating to evaluate the temporal dynamics of instabilities. This is reported in figure 18, which plots the scalogram obtained from a continuous wavelet transform of streamwise velocity fluctuations (u') on the midplane of the domain at $(x, d_n) = (6.5, 0.01)$, corresponding to a location slightly upstream of the cone–cylinder junction. The abscissa denotes non-dimensional time, while the ordinate denotes dimensional frequency in kilohertz. The red dotted line marks the cone of uncertainty. The scalogram identifies intermittent peaks at low frequencies, $f^* \sim 8-10$ kHz, which could be attributed to the unsteadiness of the above mentioned Klebanoff streaks. In addition to this low frequency, the scalogram also contains intermittent peaks

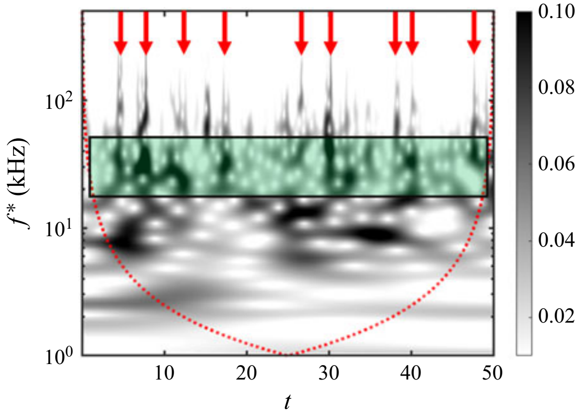

Figure 18. Scalogram of streamwise velocity fluctuations at $(x, d_n) = (6.5, 0.01)$ from DNS-H. The red dotted line marks the cone of uncertainty.

at $f^* \sim 20{-}40$ kHz (marked by the green shaded rectangle), which is in the realm of Mack's first mode instability, and show strong oblique behaviour. Such modes have also been reported in high-fidelity simulations by Hader *et al.* (2021), over a sharp cone. The appearance of first mode instability is accompanied by a broadening of the spectrum to higher frequencies, characteristic of turbulent spot formation. This suggests the potential role of intermodal interactions between the first mode and streak instabilities in driving transition in the high-amplitude perturbation environment.

The above hypothesis of first-mode/streak induced transition in DNS-H can be examined in the context of the works of Paredes, Choudhari & Li (2017) and Sharma *et al.* (2019), where it was demonstrated that steady streaks can destabilize the first mode under certain conditions, resulting in transition. Specifically, this occurs when $\lambda_{FM} < 2\lambda_{ST}$, where, λ_{FM} denotes the dominant spanwise wavelength of the first mode instability, and λ_{ST} represents the streak spacing. To compare these instability parameters from DNS-H, SPOD was conducted on the streamwise velocity fluctuations (u') over a plane parallel to the wall, offset by $d_n = 0.01$. Figure 19(*a*) illustrates the dominant modes at the two relevant frequencies identified in the scalogram (8 and 32 kHz). The mode shape at 8 kHz reveals elongated streamwise streaks resembling those shown in figure 16, with streak density increasing upstream of the expansion corner. The 32 kHz mode begins amplification at $x \sim 4$, with a highly oblique structure characteristic of the first mode instability. Figure 19(*b*) presents the azimuthal variation of the normalized mode amplitudes at $x = 6.5$, for both the above frequencies. Considering the distance between adjacent peaks or troughs as one wavelength, the 8 kHz mode display approximately five streaks, while the 32 kHz mode displays approximately seven wavelengths in the azimuthal direction within the same domain. A normalized amplitude of 0.35 is used as a threshold to identify these peaks. This indicates that twice the streak wavelength surpasses that of the first mode, promoting first mode destabilization under these conditions. The above observation was also found to be insensitive to the amplitude threshold chosen. Thus, each streak wavelength is estimated to be ∼40 % larger than the oblique first mode wavelength. When such comparable wavelengths exist, it may also induce fundamental resonance-type (Hader & Fasel 2019; Song, Dong & Zhao 2024) interactions, particularly of the type, $(1, \pm 1) \times (\sim 0, \beta) \rightarrow (1, 0)$, if $\beta \sim 1$. Here the first/second number indicates relative frequency/spanwise wavenumber. Such resonant triad interactions between oblique first modes and steady streaks can enhance the growth of two-dimensional disturbances

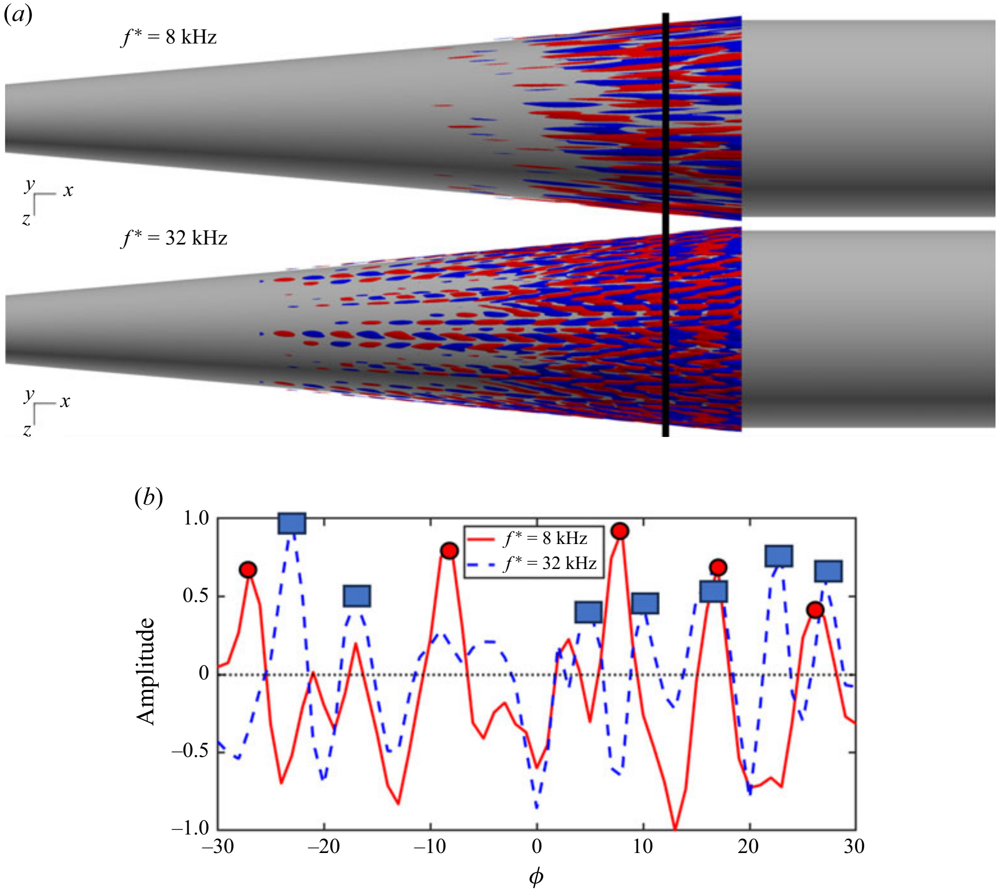

Figure 19. (*a*) Dominant SPOD mode of streamwise velocity fluctuations (u') at two specified frequencies. (*b*) Azimuthal variation of normalized amplitude of the SPOD modes at $x = 6.5$ (black solid line). Dominant peaks at $f^* = 8$ kHz are marked by red dots and peaks at $f^* = 32$ kHz are marked by blue squares.

through nonlinear coupling. In the current scenario, $\beta = 5/7$, and this interaction seems minimal, as evidenced by the modal support of the fundamental (32 kHz) in figure 19(*a*).

7. Wall loading

7.1. *Aerodynamic loading*

Due to the significant influence of transition to turbulence in creating sudden variations in aerodynamic loads, we now present a comprehensive evaluation of the mean and transient wall loading. Figure 20 presents the streamwise variation of two key parameters: wall pressure coefficient (C_p) in figure 20(*a*), and skin friction coefficient (C_f) in figure 20(*b*). It includes the laminar estimate as a baseline, along with DNS-L and DNS-H. Wall data extracted from the DNS is obtained at the mid plane of the simulation domain, after temporal averaging. Wall pressure coefficient, C_p, is calculated as

$$C_p = 2 * (p - p_\infty). \tag{7.1}$$

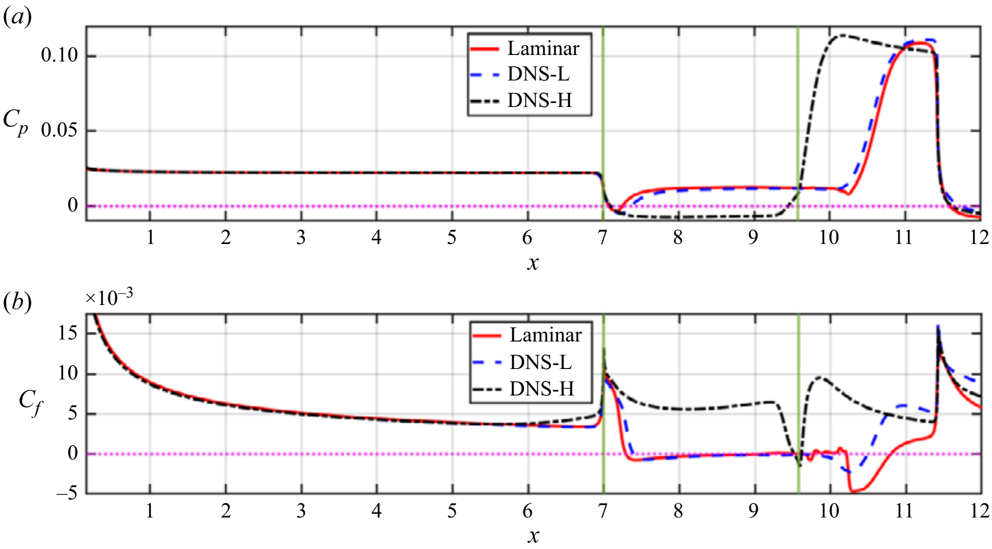

Figure 20. Streamwise variation of time averaged (*a*) wall pressure coefficient and (*b*) skin friction coefficient comparison between the laminar and the two perturbation-imposed cases. Dotted maroon line in the three plots shows the zero line. The cone–cylinder and cylinder–flare junctions are marked by the solid green lines.

Skin friction coefficient, C_f, is calculated as

$$C_f = \frac{2}{Re}\mu_w \frac{\partial u_t}{\partial d_n}\bigg|_{d_n=0}. \tag{7.2}$$

The pressure coefficient, C_p, exhibits distinct behaviour across different flow regimes. The leading-edge shock-induced rise in C_p reduces to a near-constant value over the cone in all cases, indicating its pretransitional state similar to the laminar solution. The first significant decrease in C_p at $x = 7$ coincides with the expansion fan located at the cone–cylinder junction. Flow separation and the formation of a separation bubble leads to a pressure increase in both the laminar case and DNS-L. In contrast, DNS-H exhibits a nearly constant and lower C_p along the cylinder, due to the mostly attached flow resulting from an energized boundary layer, which is resilient to separation at the cylinder–flare compression junction. However, an increase in C_p is observed at the cylinder–flare junction ($x = 9.58$) for this case. This rise is attributed to the oblique shock formed at the compression corner. Interestingly, the rise in C_p occurs farther downstream in the laminar and DNS-L cases, due to the downstream location of the mean reattachment point of the separation bubble (and hence the reattachment shock) relative to the compression corner. Finally, a pressure drop is observed across all cases at the downstream flare–cylinder junction, due to the expansion fan formed there.

Skin friction coefficient, C_f, exhibits minimal variation across the cone segment for all three cases. A slight deviation is observed in DNS-H upstream of the cone–cylinder junction, due to the earlier transition to turbulence discussed previously. Following the spike at the expansion fan at $x = 7$, the C_f values for the laminar and DNS-L cases become negative just downstream of the expansion corner. This negative value is an indicator of flow separation and the presence of a recirculation region. In DNS-L, C_f increases with the onset of transition over the flare, post reattachment ($10.5 \leqslant x \leqslant 11$), deviating it from the laminar curve. The earlier transition in DNS-H leads to significantly higher and positive C_f values over the cylinder segment ($7 \leqslant x \leqslant 10$).

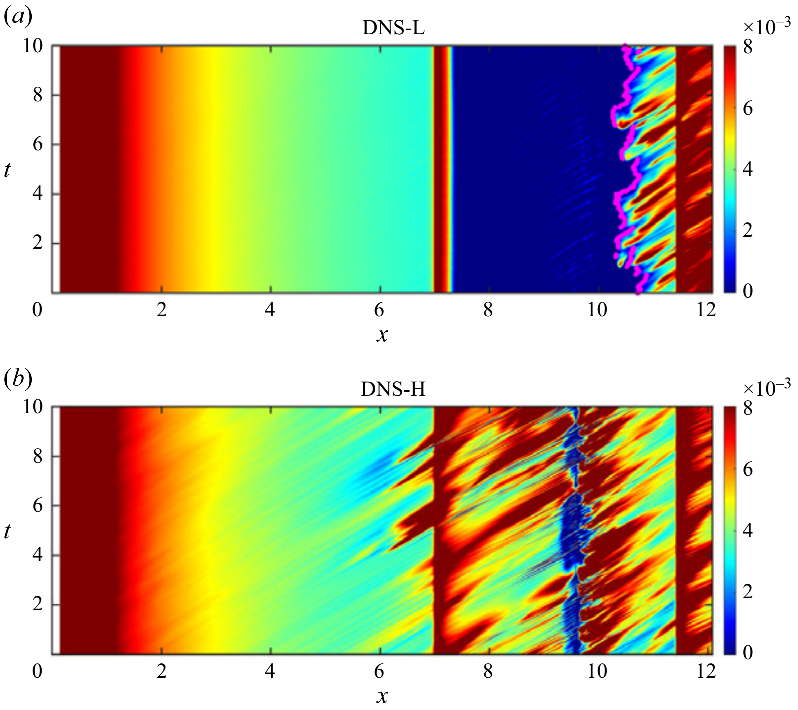

Figure 21. Space–time contours of of wall skin friction on the midplane of the DNS domain for (*a*) DNS-L and (*b*) DNS-H. The maroon line in DNS-L marks the reattachment point at a given time instant.

At the cylinder–flare junction, the presence of a compression corner results in a local dip in C_f (negative values) for DNS-H, confirming the existence of a very small separation zone at this location. While maximum skin friction in DNS-L is associated with the transition location ($x \sim 11$), that in DNS-H exists immediately downstream of the compression corner at $x \sim 10$, corresponding to the foot of the reattachment shock, as expected in SBLI systems. This highlights the sensitivity of peak wall loading in this configuration to the perturbation environment, and the resulting dominant flow physics.

In addition to the peak loading and its location, the dynamics of wall loading are also different in DNS-L and DNS-H, as evidenced by its temporal signature. Figures 21(*a*) and 21(*b*) show the temporal variation of skin friction along the length of the CCF geometry at the midplane of the domain, for DNS-L and DNS-H, respectively. The laminar flow over the cone, as well as the separation point downstream of the cone–cylinder junction, exhibit negligible unsteadiness in DNS-L. However, the reattachment point has significant temporal variation. Reattachment points are identified as inflection points in wall tangential velocity in the vicinity of the mean reattachment point, and are shown in figure 21(*a*) using a maroon line. Statistics of these reattachment points were observed to be sporadic without any discernible periodicity and very small temporal integral length scales. This is primarily due to the fact that, these undulations result from the nonlinear manifestation of the stationary global streak instability of the bubble. Post reattachment, intermittent peaks in C_f are observed, as the boundary layer increasingly becomes transitional due to the secondary instabilities of the streaks. An interesting observation in these contours is that, peaks in C_f are preceded by an upstream shift in

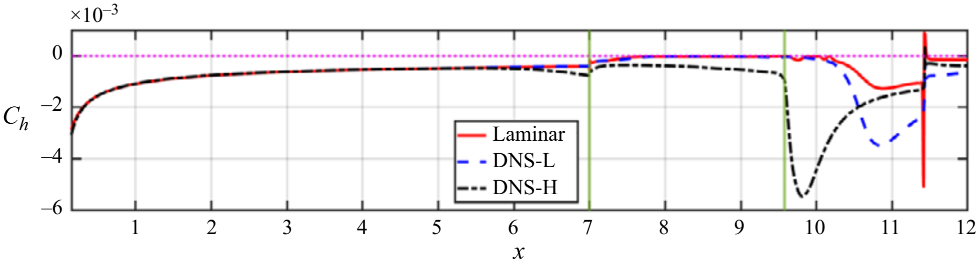

Figure 22. Streamwise variation of time averaged heat transfer coefficient. Dotted maroon line shows the zero line. The cone–cylinder and cylinder–flare junctions are marked by the solid green lines.

the local reattachment point, due to the streak instabilities energizing the boundary layer near the reattachment zone.

Temporal unsteadiness of skin friction in DNS-H (figure 21*b*) is qualitatively different. In addition to the upstream shift of transition location resulting in regions of high C_f over the cylinder segment, their peak values become comparable to those seen within the fully turbulent boundary layer downstream of the compression corner at the flare–cylinder junction. Each major skin friction event over the cylinder and flare segments can be traced upstream to the cone segment, where the intermodal interaction of the streak and first mode instabilities generates turbulent spots that convect downstream. As these turbulized packets cross the cylinder–flare junction, it collapses the small separation bubble. Although not shown for brevity, every single precursor-peak in C_f over the cone at $x \sim 6$ can be associated with an intermittent energization of the first mode in the vicinity of $f^* = 32$ kHz, (see e.g. figure 18).

7.2. *Thermal loading*

Thermal loading is quantified via surface heat transfer coefficient, C_h, which is calculated as

$$C_h = -\frac{\mu_w}{RePr}\frac{1}{(T_r - T_w)}\frac{\partial \mathrm{T}}{\partial d_n}\bigg|_{d_n=0}. \tag{7.3}$$

Recovery temperature, T_r, is defined as

$$T_r = 1 + \tilde{r}\frac{\gamma - 1}{2}M_\infty^2, \tag{7.4}$$

with recovery factor, $\tilde{r} = Pr^{1/3}$. This yields a ratio of $T_w/T_r \sim 0.8$.

Figure 22 compares mean C_h as predicted in the laminar and transitional simulations. Negative values of C_h are indicative of heat transfer into the wall from the flow field. The trends are similar to those seen in the skin friction coefficient (C_f) in figure 20(*b*). Over the cone segment, C_h distribution is identical across all cases. Deviations appear in DNS-H due to the earlier transition to turbulence. The isentropic expansion waves have a relatively lower impact on the thermal loading in contrast to the compression corner, which leads to a sharp rise in C_h, particularly for the fully turbulized boundary layer in DNS-H. Peak C_h in DNS-H also coincides with the SBLI zone of the reattachment shock, as seen in the corresponding C_f trends. In DNS-L, the increase in C_h following reattachment on the flare region is substantially higher than that seen in the laminar case, due to the transitional nature of the flow at this location. The lower intermittency and near-wall gradients of transitional events in DNS-L compared with DNS-H, particularly over the flare (evident in figure 21), results in the former displaying lower peak values in the time averaged C_h plot.

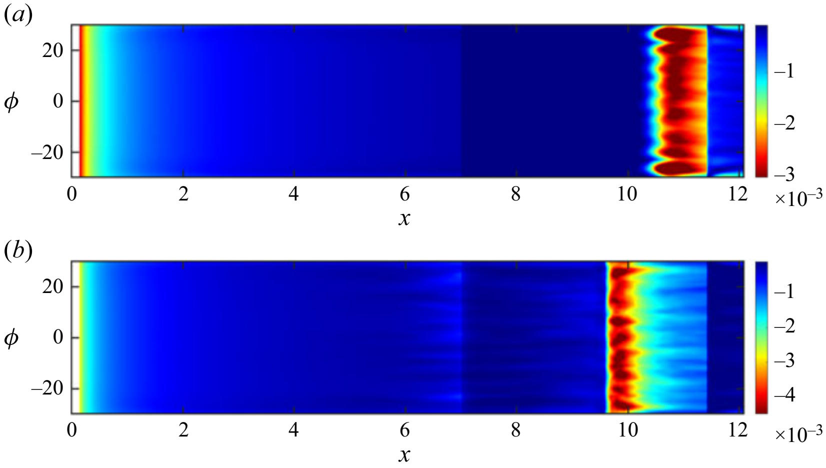

Figure 23. Contours of time averaged surface heat transfer coefficient for (*a*) DNS-L and (*b*) DNS-H.

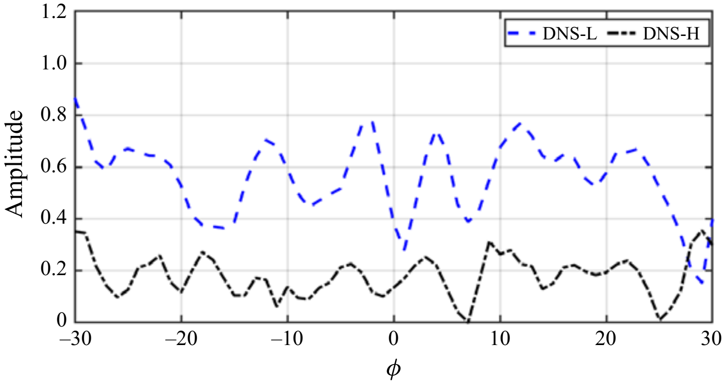

Figure 24. Comparison of azimuthal variation of time averaged and normalized heat transfer coefficient between the DNS-L and DNS-H cases. Surface variation of C_h is extracted at $x = 10.6$ from DNS-L and $x = 9.7$ from DNS-H.

Figure 23 presents time-averaged surface heat transfer coefficient contours for the two DNS cases, to demonstrate azimuthal inhomogeneity post transition. In DNS-L (figure 23*a*), C_h streak patterns emerge downstream of reattachment (Roghelia *et al.* 2017; Chuvakhov *et al.* 2021), consistent with the spanwise wavenumber of the global streak instability of the separation bubble, as verified earlier in figure 15. However, in DNS-H (figure 23*b*), the dominant azimuthal wavenumber visible in C_h is different. This is further quantified in figure 24, which compares the azimuthal variation of time averaged normalized heat transfer coefficients from DNS-L and DNS-H. Azimuthal variation of C_h is extracted at $x = 10.6$ from DNS-L, and $x = 9.7$ from DNS-H, which corresponds to their respective peak locations, as evident in figure 23. The plot shows around seven dominant peaks from DNS-L in the 60° sector, while at least nine peaks are visible in the DNS-H, which was confirmed through an azimuthal Fourier decomposition of these signals. This suggests that peak wall loading in DNS-H is induced by streaks with relatively shorter spanwise wavelengths.

This difference in dominant wavenumber suggests a different underlying mechanism driving region of peak thermal loading in DNS-H. Although not shown for brevity,

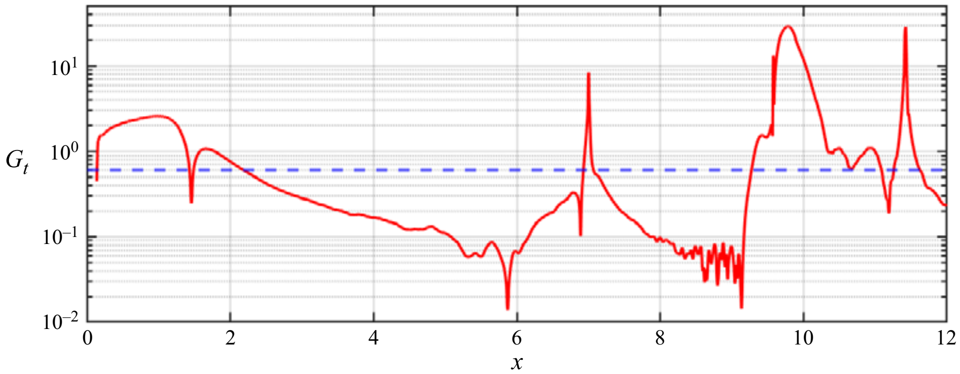

Figure 25. Streamwise variation of local Görtler number at a distance of $d_n = 0.01$ from the wall. The blue dashed line marks the threshold of 0.6, above which Görtler vortices are observed.

additional linear analyses were conducted to ensure that the basic state obtained from DNS-H does not sustain an absolute instability at the cylinder–flare junction. Roghelia *et al.* (2017) and Chuvakhov *et al.* (2021) have proposed that Görtler-type vortices may result in such near-wall streaks. Further, research by Viaro & Ricco (2019*a*,*b*) and Sescu, Afsar & Hattori (2020) has demonstrated that laminar boundary layers can entrain unsteady free stream vortical disturbances, leading to the formation of Klebanoff modes, which can then evolve into Görtler vortices downstream. This progression is described in detail by Xu, Ricco & Duan (2024). Therefore, the above hypothesis is investigated here by examining the streamwise evolution of the local Görtler number within the boundary layer. The local Görtler number (Xu *et al.* 2024) is calculated as

$$G_t = \frac{u_\infty^* \theta^*}{\nu^*}\sqrt{\frac{\theta^*}{r_0^*}} \tag{7.5}$$

where, θ^* is the momentum thickness of the boundary layer, and r_0^* is the radius of curvature of the surface. Since the current geometry includes a sharp compression corner, the radius of curvature is calculated as

$$r_0 = \frac{1}{\kappa}, \quad \kappa = \frac{\left[u^2\frac{\partial v}{\partial x} - v^2\frac{\partial u}{\partial y} + uv\left(\frac{\partial v}{\partial y} - \frac{\partial u}{\partial x}\right)\right]}{\left(u^2+v^2\right)^{3/2}}, \tag{7.6}$$

following Tong *et al.* (2017). It has to be noted that the above formula is applied to the time-averaged flow field.

Figure 25 plots the streamwise evolution of the local Görtler number at a distance of $d_n = 0.01$ from the wall. The blue dashed line indicates the critical threshold of 0.6, as noted by several studies (Tong *et al.* 2017; Khobragade, Unnikrishnan & Kumar 2022; Xu *et al.* 2024), above which Görtler vortices are typically observed. Except for abrupt spikes near the expansion and compression corners (resulting from rapid geometric changes), the data show that the Görtler number primarily peaks significantly within the small separation zone at the cylinder–flare junction ($9.5 \leqslant x \leqslant 10.5$). At this location, the Görtler number is nearly an order of magnitude above the threshold, suggesting a strong likelihood for the generation of Görtler vortices in this region.

Figure 26 demonstrates the impact of Görtler vortices by displaying the mean surface imprint of streamwise vorticity (ω_x), along with contours of streamwise velocity to highlight the separation zone. The velocity contours in figure 26 show that the effective

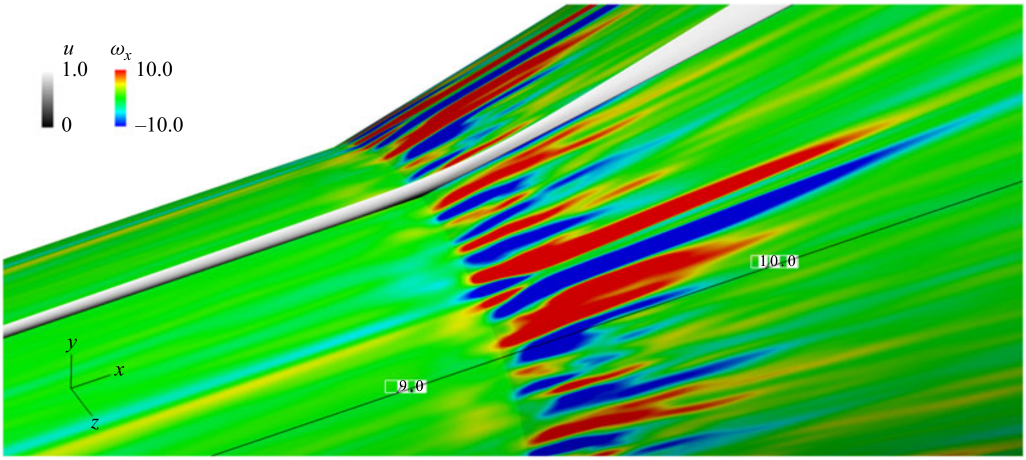

Figure 26. Surface contours of mean streamwise vorticity (ω_x) obtained from DNS-H. Also included are contours of streamwise velocity to highlight the separation zone.

curvature at the compression corner is significantly larger in DNS-H compared with DNS-L, as shown earlier in figure 12, due to the almost attached nature of flow in the former. This is also evident by tracking the edge of boundary layer and the separating shear layer over the cylinder and flare in figure 5(*b,c*), which compares mean flow features across various cases. This results in the sudden increase in Görtler number, as seen in figure 25. The vorticity contours highlight streamwise vortices emerging near the cylinder–flare region, where the Görtler number peaks. These vortices significantly impact the flow up to approximately $x \sim 10.5$, and exist in regions where peak heat transfer coefficient values were identified in figure 23, which was confirmed by comparing the near-wall values of streamwise vorticity and heat transfer coefficient. This demonstrates the role of Görtler vortices on the formation of skin friction and heat transfer streaks in environments with high free stream perturbations. It is, however, important to note that, due to the higher inflow turbulence intensity in DNS-H, the initial amplitudes of unsteady modes are higher than that of steady modes, resulting in the dominance of unsteady Görtler vortices which may not have an imprint in a very long time-averaged flow field, when compared with steady Görtler modes, that often dominate laminar flows with low free stream perturbation levels (Li *et al.* 2022). The above analyses thus underscore the substantial influence of free stream conditions through boundary layer transition mechanisms, on wall loading over geometries sustaining multimodal dynamics.

8. Conclusions

This study investigates the influence of free stream disturbance amplitude on the dynamics and transition mechanisms in HBLs over a CCF geometry. A global linear stability approach, termed the NS-MFP, and DNS are utilized for the linear and nonlinear analyses, respectively. Comparisons are first drawn between the laminar solution and time-averaged basic states of two DNS predictions, DNS-L and DNS-H, which corresponds to the CCF flow fields under relatively quiet and noisy conditions, respectively. The laminar solution and DNS-L show significant similarities, characterized by a large separation region that originates downstream of the cone–cylinder junction, and terminates midway over the flare. The boundary layer undergoes transition post reattachment in DNS-L. In contrast, DNS-H reveals a predominantly attached boundary layer, with a small separation zone at the cylinder–flare compression corner. In addition, there is an upstream shift in transition onset, resulting in a fully turbulent boundary layer at the cylinder–flare junction.

To identify the transition mechanism in DNS-L (quieter environment), a global stability analysis is performed on the laminar basic state, due to the resemblance between the two cases. This reveals multiple convective instabilities, including Mack's first mode (35 kHz) and second mode (272 kHz), over the cone segment. The shear layer over the separation bubble also sustains K-H instabilities that eventually propagate over the flare segment. The NS-MFP also identifies an absolute instability within the separation bubble, with peak amplitude near the reattachment zone. It manifests spatially in the form of streamwise streaks with an azimuthal wavenumber of $m = 21$, and the instability eigenspectrum reveals that this is a stationary instability with positive temporal growth rate. As confirmed in DNS-L, streak formation by this absolute instability, and its eventual nonlinear saturation and secondary instabilities, drive transition under low-amplitude perturbation environments. The first mode within the 20–50 kHz range appears as oblique disturbances that amplify over the cone boundary layer, and later through the shear layer over the separation. Conversely, the second mode attenuates in the shear layer, and the K-H bands show the characteristic $1/x$ decay. At elevated free stream disturbance amplitudes, DNS-H indicates that the transition mechanism is qualitatively different, with bypass transition having a major role. This is marked by intermittent amplification of streamwise streaks resembling Klebanoff modes, over the cone segment. An interaction between streamwise streaks and oblique first modes results in destabilization of the latter, producing convecting turbulent spots and intermittent breakdown near the cone–cylinder junction. Furthermore, spanwise-invariant rollers were observed over the cylinder segment, corresponding to energetic high-frequency content ($\sim$350 kHz) in the wall pressure spectra, consistent with the frequency range of Mack's second mode.

Mean and time-accurate surface flow analyses are performed to quantify aerothermal loading resulting from transition. Increased free stream disturbance amplitude causes a substantial rise and upstream shift in peak wall-normal, shear and thermal loading, due to an earlier transition onset. In DNS-L, the reattachment point over the flare exhibits strong spatiotemporal fluctuations in skin friction coefficient (C_f), whereas DNS-H displays intermittent streaks of increased C_f, linked to convecting turbulent spots. Thermal streaks appear postreattachment in DNS-L, and postcompression in DNS-H. The former is attributed to the absolute instability within the separation region, while the latter result from unsteady Görtler vortices near the cylinder–flare junction, driven by high local curvature. These inferences underscore the significance of free stream disturbance environment in defining transition pathways and aerothermal loading in multimodal hypersonic flows.

Funding. This research was supported by the Office of Naval Research, through grant no. N00014-21-1-2408, monitored by Dr E. Marineau.

Declaration of interests. The authors report no conflict of interest.

Appendix A. Digital-filter-based noise generation

To provide free stream perturbations, spatiotemporally correlated pressure and velocity perturbations, simulated using the digital filter approach Adler *et al.* (2018), are introduced as Dirichlet BCs at the inflow plane. Qualitatively, this mode of forcing introduces vortical, acoustic and entropic perturbations in the inflow disturbance field. Specifically, for any inflow variable, ϕ, the Dirichlet condition is set as $\phi = \phi_\infty + \phi'$, where, ϕ_∞ are the steady free stream conditions, and ϕ' is the perturbation obtained from the digital filter.

The synthetic digital filtering method is initiated with random fluctuations, whose values are low-pass filtered in space/time to enforce approximate integral length/time scales. Two normally distributed random number sequences (r_j) are first obtained. Using two-dimensional exponential spatial filters, these random sequences are filtered to roughly represent the integral length scales in the transverse and spanwise directions. The following is the filter window function across the inflow plane (y, z) for each spatial location (y_o, z_o):

$$w(y, z; y_o, z_o) = \frac{1}{\alpha} \exp\left(-\sqrt{\left(\frac{y - y_o}{I_y(y_o, z_o)}\right)^2 + \left(\frac{z - z_o}{I_z(y_o, z_o)}\right)^2}\right), \tag{A1}$$

where α is a normalization for the filter to have unit integral over the whole domain ($\int w(y, z; y_o, z_o)^2 \mathrm{d}y\mathrm{d}z = 1$), and I_y and I_z represent the specified transverse and spanwise integral length scales at the seed points (y_o, z_o). In discrete form, the filter is implemented as

$$w(j, k; j_o, k_o) = \frac{1}{\alpha} \exp\left(-\sqrt{\left(\frac{j - j_o}{I_y(j_o, k_o)}\right)^2 + \left(\frac{k - k_o}{I_z(j_o, k_o)}\right)^2}\right). \tag{A2}$$

By performing the convolution solely across a small neighbourhood surrounding the seed point, computational overhead is minimized $|j - j_o| < 2\pi I_j(j_o, k_o) \equiv N_j$ and $|k - k_o| < 2\pi I_k(j_o, k_o) \equiv N_k$. Thus, the filtering operation is given as

$$\eta_{it}(j_o, k_o) = \sum_{j=j_o-N_j}^{j_o+N_j} \sum_{k=k_o-N_k}^{k_o+N_k} w(j, k; j_o, k_o) r_i(j, k), \tag{A3}$$

and are used to create a new spatially filtered random sequence over the inflow domain $\eta_{it}(j, k)$ at each time step (t).

To introduce the integral time scales, the spatially filtered random numbers (η_{it}) are subsequently temporally filtered. This is performed using the method specified by Xie & Castro (2008) as

$$\epsilon_i(j, k, t + \Delta t) = \epsilon_i(j, k, t)\sqrt{\exp\left(-\frac{\Delta t}{I_t(j, k)}\right)} + \eta_{it}(j, k)\sqrt{1 - \exp\left(-\frac{\Delta t}{I_t(j, k)}\right)}. \tag{A4}$$

The spatially correlated random fields ($\eta_{it}(j, k)$) are thus converted into temporally correlated fields as well ($\epsilon_i(j, k, t)$). Taylor's hypothesis ($I_t = I_x/U$), is used to calculate the integral time scale, where I_x is the streamwise integral length scale and $U(y, z)$ is the streamwise velocity scale. The integral length scales, I_y and I_z, are prescribed with the assumption that they are equal along the inflow plane. Values of $I_x = 0.05$ and $I_y = I_z = 0.01$ are used in the current study. The flow response was found to be similar to variations in these quantities across an order of magnitude.

The PSD of streamwise velocity fluctuations (u') in the free stream at the inflow plane for the DNS-L and H cases is shown in figure 27. Peak PSD levels of $\sim 10^{-6}$ in DNS-H and $\sim 10^{-8}$ in DNS-L are consistent with r.m.s. levels of 0.1 % and 0.01 % of free stream velocity. Energy is predominant at lower frequencies ($f^* \leqslant 100$ kHz) due to the low-pass nature of the filtering. This spectrum aligns well with the free stream Pitot-pressure fluctuations measured in multiple high-speed facilities, as reported in Duan *et al.* (2019).

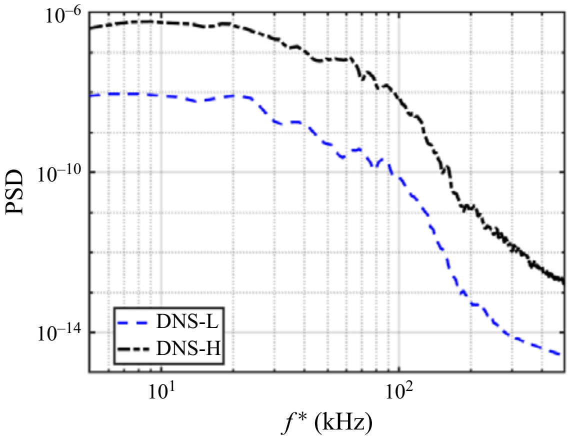

Figure 27. Comparison of power spectral density (PSD) of free stream velocity fluctuations obtained from the digital filtering approach, imposed at the inflow plane.

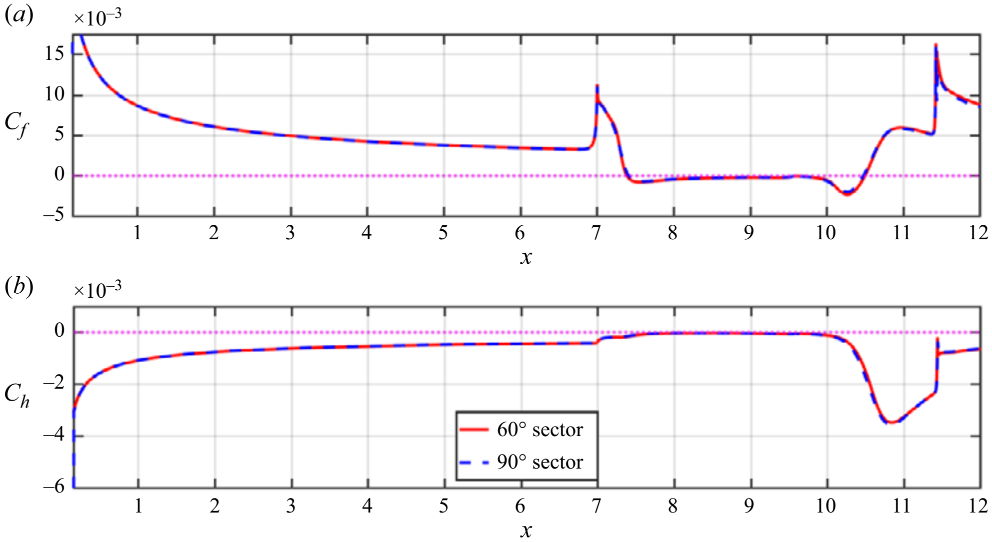

Figure 28. Streamwise variation of time and spanwise averaged (*a*) skin friction coefficient and (*b*) heat transfer coefficient. Dotted maroon line shows the zero line.

Appendix B. Domain independence study

As mentioned in § 3, to ensure that the key inferences made are not affected by the choice of the finite sector computations, a domain independence study is conducted as summarized here. For this purpose, results from DNS-L (with low free stream perturbation amplitude) are compared, as obtained from two simulations performed on a 90° sector and a 60° sector. The grid spacing remains identical in both cases, with 121 and 181 nodes used to resolve the 60° and 90° sectors, respectively.

Figure 28(*a*,*b*) compares the streamwise variation of spanwise and temporally averaged surface skin friction coefficient (C_f) and heat transfer coefficient, respectively, between the 60° and 90° sector simulations. The mean separation and reattachment points align

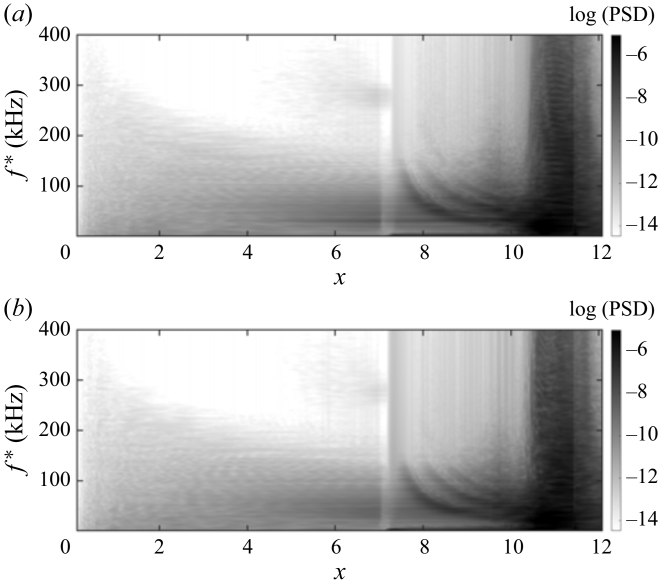

Figure 29. Streamwise variation of wall pressure spectra obtained from (*a*) 60° sector DNS and (*b*) 90° sector DNS.

closely between the two simulations. The mean loading experienced by the surface is also identical between the two cases.

Figure 29(*a*,*b*) compares unsteady features using the wall pressure spectra at the $\phi = 0$ plane, obtained from the 60° and 90° sector DNS, respectively. The nature of the convective instabilities, amplification of low-frequency first mode and high-frequency second mode, as well as onset and streamwise scaling of shear layer instabilities are consistent between the two simulations. Downstream of the reattachment, the onset of breakdown and spectral broadening are also comparable in both simulations.

REFERENCES

ADAMCZAK, D., ALESI, H. & FROST, M. 2009 HIFiRE-1: payload design, manufacture, ground test, and lessons learned. In *16th AIAA/DLR/DGLR International Space Planes and Hypersonic Systems and Technologies Conference*, pp. 7294. American Institute of Aeronautics and Astronautics (AIAA).

ADAMS, N.A. 2001 Direct numerical simulation of transition in compressible flows. In *DNS/LES Progress and Challenges*, (eds. C. LIU, L. SAKELL & T. BEUTNER), pp. 171–182. Greyden Press.

ADLER, M.C., GONZALEZ, D.R., STACK, C.M. & GAITONDE, D.V. 2018 Synthetic generation of equilibrium boundary layer turbulence from modeled statistics. *Comput. Fluids* **165**, 127–143.

ANDERSSON, P., BERGGREN, M. & HENNINGSON, D.S. 1999 Optimal disturbances and bypass transition in boundary layers. *Phys. Fluids* **11** (1), 134–150.

ANDERSSON, P., BRANDT, L., BOTTARO, A. & HENNINGSON, D.S. 2001 On the breakdown of boundary layer streaks. *J. Fluid Mech.* **428**, 29–60.

ANDREWS, G. & POGGIE, J. 2020 Effects of freestream acoustic disturbances on hypersonic boundary layer stability. In *AIAA Aviation 2020 Forum*, pp. 2995. American Institute of Aeronautics and Astronautics (AIAA).

ARAYA, G., LAGARES, C.J., SANTIAGO, J. & JANSEN, K.E. 2021 Wall temperature effect on hypersonic turbulent boundary layers via dns. In *AIAA Scitech 2021 Forum*, pp. 1745. American Institute of Aeronautics and Astronautics (AIAA).

ASWATHY NAIR, K. & UNNIKRISHNAN, S. 2024 Effects of nose bluntness on hypersonic transition over ogive-cylinder forebodies. *AIAA J.* **62** (2), 476–488.

BALAKUMAR, P. 2015 Receptivity of hypersonic boundary layers to acoustic and vortical disturbances. In *45th AIAA Fluid Dynamics Conference*, pp. 2473. American Institute of Aeronautics and Astronautics (AIAA).

BALAKUMAR, P. & CHOU, A. 2018 Transition prediction in hypersonic boundary layers using receptivity and freestream spectra. *AIAA J.* **56** (1), 193–208.

BALAKUMAR, P., ZHAO, H. & ATKINS, H. 2005 Stability of hypersonic boundary layers over a compression corner. *AIAA J.* **43** (4), 760–767.

BEAM, R. & WARMING, R. 1978 An implicit factored scheme for the compressible Navier–Stokes equations. *AIAA J.* **16** (4), 393–402.

BECKER, J.V. & KORYCINSKI, P.F. 1962 Heat transfer and pressure distribution at a Mach number of 6.8 on bodies with conical flares and extensive flow separation, Tech. Rep., NACA.

BENITEZ, E.K., 2024 Separation and transition on a cone-cylinder-flare: experimental campaigns. In *AIAA SciTech 2024 Forum*, pp. 0496. American Institute of Aeronautics and Astronautics (AIAA).

BENITEZ, E.K., BORG, M.P., PAREDES, P., SCHNEIDER, S.P. & JEWELL, J.S. 2023*a* Measurements of an axisymmetric hypersonic shear-layer instability on a cone-cylinder-flare in quiet flow. *Phys. Rev. Fluids* **8** (8), 083903.

BENITEZ, E.K., BORG, M.P., SCHOLTEN, A., PAREDES, P., MCDANIEL, Z. & JEWELL, J.S. 2023*b* Instability and transition onset downstream of a laminar separation bubble at Mach 6. *J. Fluid Mech.* **969**, A11.

BENITEZ, E.K., ESQUIEU, S., JEWELL, J.S. & SCHNEIDER, S.P. 2020 Instability measurements on an axisymmetric separation bubble at Mach 6. In *AIAA Aviation 2020 Forum*, pp. 3072. American Institute of Aeronautics and Astronautics (AIAA).

CAILLAUD, C., 2024 Separation and transition on a cone-cylinder-flare: computational investigations. In *AIAA Scitech 2024 Forum*, pp. 0497. American Institute of Aeronautics and Astronautics (AIAA).

CHOU, A., WARD, C., LETTERMAN, L., SCHNEIDER, S., LUERSEN, R. & BORG, M. 2011 Transition research with temperature-sensitive paints in the Boeing/AFOSR Mach-6 quiet tunnel. In 41st AIAA Fluid Dynamics Conference and Exhibit, pp. 3872.

CHUVAKHOV, P.V., EGOROV, I.V., ILYUKHIN, I.M., OBRAZ, A.O., FEDOROV, A.V. & FEDOROV, A.V. 2021 Boundary-layer instabilities in supersonic expansion corner flows. *AIAA J.* **59** (9), 3398–3405.

DUAN, L., 2019 Characterization of freestream disturbances in conventional hypersonic wind tunnels. *J. Spacecr. Rockets* **56** (2), 357–368.

DWIVEDI, A., SIDHARTH, G.S., NICHOLS, J.W., CANDLER, G.V. & JOVANOVIĆ, M.R. 2019 Reattachment streaks in hypersonic compression ramp flow: an input–output analysis. *J. Fluid Mech.* **880**, 113–135.

FAN, J., HAO, J. & WEN, C.-Y. 2022 Nonlinear interactions of global instabilities in hypersonic laminar flow over a double cone. *Phys. Fluids* **34** (12), 126108.

FASEL, H.F. 2002 Numerical investigation of the interaction of the Klebanoff-mode with a Tollmien–Schlichting wave. *J. Fluid Mech.* **450**, 1–33.

GINOUX, J. 1965 Investigation of flow separation over ramps at M = 3, Tech. Rep. AEDC-TR-65-273, Von Karman Gas Dynamics Facility, Arnold Engineering Development Center.

GOLDSTEIN, M.E. 2014 Effect of free-stream turbulence on boundary layer transition. *Phil. Trans. R. Soc. A: Math. Phys. Engng Sci.* **372**(2020), 20130354.

GOPARAJU, H., UNNIKRISHNAN, S. & GAITONDE, D.V. 2021 Effects of nose bluntness on hypersonic boundary-layer receptivity and stability. *J. Spacecr. Rockets* **58** (3), 668–684.

GUO, P., SHI, F., GAO, Z., JIANG, C., LEE, C.-H. & WEN, C. 2022 Heat transfer and behavior of the Reynolds stress in Mach 6 boundary layer transition induced by first-mode oblique waves. *Phys. Fluids* **34** (10), 104116.

GUTMARK, E.J. & HO, C.-M. 1983 Preferred modes and the spreading rates of jets. *Phys. Fluids* **26** (10), 2932–2938.

HACK, M.J.P. & ZAKI, T.A. 2014 Streak instabilities in boundary layers beneath free-stream turbulence. *J. Fluid Mech.* **741**, 280–315.

HADER, C., DENG, N. & FASEL, H.F. 2021 Direct numerical simulations of hypersonic boundary-layer transition for a straight cone at Mach 5. In *AIAA Scitech 2021 Forum*, pp. 0743. American Institute of Aeronautics and Astronautics (AIAA).

HADER, C. & FASEL, H.F. 2019 Direct numerical simulations of hypersonic boundary-layer transition for a flared cone: fundamental breakdown. *J. Fluid Mech.* **869**, 341–384.

HELMHOLTZ, H.V. 1868 On discontinuous movements of fluids. *Lond. Edinburgh Dublin Phil. Mag. J. Sci.* **36** (244), 337–346.

HO, C.-M. & HUERRE, P. 1984 Perturbed free shear layers. *Annu. Rev. Fluid Mech.* **16**, 365–424.

HUNT, J.C.R. & DURBIN, P.A. 1999 Perturbed vortical layers and shear sheltering. *Fluid Dyn. Res.* **24** (6), 375.

HUSSAIN, A.K.M.F. 1986 Coherent structures and turbulence. *J. Fluid Mech.* **173**, 303–356.

JACOBS, R.G. & DURBIN, P.A. 2001 Simulations of bypass transition. *J. Fluid Mech.* **428**, 185–212.

JAMESON, A., SCHMIDT, W. & TURKEL, E. 1981 Numerical solution of the Euler equations by finite volume methods using Runge–Kutta time stepping schemes. In *14th Fluid and Plasma Dynamics Conference*, pp. 1259. American Institute of Aeronautics and Astronautics (AIAA).

KHOBRAGADE, N., UNNIKRISHNAN, S. & KUMAR, R. 2022 Flow instabilities and impact of ramp–isolator junction on shock–boundary-layer interactions in a supersonic intake. *J. Fluid Mech.* **953**, A30.

KIMMEL, R.L. & PRABHU, D.K. 2015 HIFiRE-1 turbulent shock boundary layer interaction-flight data and computations. In *45th AIAA Fluid Dynamics Conference*, pp. 2639. American Institute of Aeronautics and Astronautics (AIAA).

LAKSHMI NARASIMHA PRASAD, A. & UNNIKRISHNAN, S. 2024 Noise mitigation in rectangular jets through plasma actuator-based shear layer control. *J. Fluid Mech.* **979**, A16.

LANDAHL, M.T. 1980 A note on an algebraic instability of inviscid parallel shear flows. *J. Fluid Mech.* **98** (2), 243–251.

LI, X., ZHANG, Y., YU, H., LIN, Z.-K., TAN, H.-J. & SUN, S. 2022 Görtler vortices behavior and prediction in dual-incident shock-wave/turbulent-boundary-layer interactions. *Phys. Fluids* **34** (10), 106103.

LUGRIN, M., BENEDDINE, S., LECLERCQ, C., GARNIER, E. & BUR, R. 2021 Transition scenario in hypersonic axisymmetrical compression ramp flow. *J. Fluid Mech.* **907**, A6.

MACK, L.M. 1984 Boundary-layer linear stability theory. *Agard. Rep.* **709** (3), 1–3.

MACK, L.M. 1990 On the inviscid acoustic-mode instability of supersonic shear flows: Part 1: two-dimensional waves. *Theor. Comput. Fluid Dyn.* **2** (2), 97–123.

MANDAL, A.C., VENKATAKRISHNAN, L. & DEY, J. 2010 A study on boundary-layer transition induced by free-stream turbulence. *J. Fluid Mech.* **660**, 114–146.

MATSUBARA, M. & ALFREDSSON, P.H. 2001 Disturbance growth in boundary layers subjected to free-stream turbulence. *J. Fluid Mech.* **430**, 149–168.

MICHALKE, A. 1965 On spatially growing disturbances in an inviscid shear layer. *J. Fluid Mech.* **23** (3), 521–544.

MORKOVIN, M.V. 1985 *Bypass Transition to Turbulence and Research Desiderata*. NASA. Lewis Research Center Transition in Turbines.

MORKOVIN, M.V. 1994 Transition in open flow systems-a reassessment. *Bull. Am. Phys. Soc.* **39**, 1882.

OVCHINNIKOV, V., CHOUDHARI, M.M. & PIOMELLI, U. 2008 Numerical simulations of boundary-layer bypass transition due to high-amplitude free-stream turbulence. *J. Fluid Mech.* **613**, 135–169.

PAREDES, P., CHOUDHARI, M.M., LI, F., JEWELL, J.S., KIMMEL, R.L., MARINEAU, E.C. & GROSSIR, G. 2018 Nosetip bluntness effects on transition at hypersonic speeds: experimental and numerical analysis under NATO STO AVT-240. In *2018 AIAA Aerospace Sciences Meeting*, pp. 0057. American Institute of Aeronautics and Astronautics (AIAA).

PAREDES, P., CHOUDHARI, M.M. & LI, F. 2017 Instability wave–streak interactions in a supersonic boundary layer. *J. Fluid Mech.* **831**, 524–553.

PAREDES, P., SCHOLTEN, A., CHOUDHARI, M.M., LI, F., BENITEZ, E.K. & JEWELL, J.S. 2022 Boundary-layer instabilities over a cone–cylinder–flare model at Mach 6. *AIAA J.* **60** (10), 5652–5661.

PULLIAM, T.H. & CHAUSSEE, D.S. 1981 A diagonal form of an implicit approximate-factorization algorithm. *J. Comput. Phys.* **39** (2), 347–363.

RANJAN, R., UNNIKRISHNAN, S. & GAITONDE, D.V. 2020 A robust approach for stability analysis of complex flows using high-order Navier–Stokes solvers. *J. Comput. Phys.* **403**, 109076.

RANJAN, R., UNNIKRISHNAN, S., ROBINET, J.-C. & GAITONDE, D.V. 2021 Global transition dynamics of flow in a lid-driven cubical cavity. *Theor. Comput. Fluid Dyn.* **35**, 397–418.

RESHOTKO, E. 1976 Boundary-layer stability and transition. *Annu. Rev. Fluid Mech.* **8** (1), 311–349.

ROE, P.L. 1981 Approximate riemann solvers, parameter vectors and difference schemes. *J. Comput. Phys.* **43**, 357–372.

ROGHELIA, A., OLIVIER, H., EGOROV, I. & CHUVAKHOV, P. 2017 Experimental investigation of Görtler vortices in hypersonic ramp flows. *Exp. Fluids* **58**, 1–15.

SANDBERG, R.D. 2007 Governing equations for a new compressible Navier–Stokes solver in general cylindrical coordinates. AFM-07/07. School of Engineering Sciences, University of Southampton.

SCHMID, P.J. 2010 Dynamic mode decomposition of numerical and experimental data. *J. Fluid Mech.* **656**, 5–28.

SCHMIDT, O.T. & COLONIUS, T. 2020 Guide to spectral proper orthogonal decomposition. *AIAA J.* **58** (3), 1023–1033.

SCHNEIDER, S.P. 2008 Effects of roughness on hypersonic boundary-layer transition. *J. Spacecr. Rockets* **45** (2), 193–209.

SESCU, A., AFSAR, M. & HATTORI, Y. 2020 Streaks in high-speed boundary layers: a view through the full nonlinear boundary-region equations. In *AIAA Scitech 2020 Forum*, pp. 0830. American Institute of Aeronautics and Astronautics (AIAA).

SHARMA, S., SHADLOO, M.S., HADJADJ, A. & KLOKER, M.J. 2019 Control of oblique-type breakdown in a supersonic boundary layer employing streaks. *J. Fluid Mech.* **873**, 1072–1089.

SHI, M., XU, L., WANG, Z. & LV, H. 2019 Effect of a roughness element on the hypersonic boundary layer receptivity due to different types of free-stream disturbance with a single frequency. *Entropy* **21** (3), 255.

SHU, C.W. & OSHER, S. 1988 Efficient implementation of essentially non-oscillatory shock-capturing schemes. *J. Comput. Phys.* **77** (2), 439–471.

SIDHARTH, G.S., DWIVEDI, A., CANDLER, G.V. & NICHOLS, J.W. 2018 Onset of three-dimensionality in supersonic flow over a slender double wedge. *Phys. Rev. Fluids* **3** (9), 093901.

SIVASUBRAMANIAN, J. & FASEL, H. 2011 Transition initiated by a localized disturbance in a hypersonic flat-plate boundary layer. In *49th AIAA Aerospace Sciences Meeting including the New Horizons Forum and Aerospace Exposition*, pp. 374. American Institute of Aeronautics and Astronautics (AIAA).

SONG, R., DONG, M. & ZHAO, L. 2024 Principle of fundamental resonance in hypersonic boundary layers: an asymptotic viewpoint. *J. Fluid Mech.* **978**, A30.

STETSON, K. 1983 Nosetip bluntness effects on cone frustum boundary layer transition in hypersonic flow. In *16th Fluid and Plasmadynamics Conference*, pp. 1763. American Institute of Aeronautics and Astronautics (AIAA).

SWANSON, R.C. & TURKEL, E. 1992 On central-difference and upwind schemes. *J. Comput. Phys.* **101** (2), 292–306.

THOMSON, W. 1871 Hydrokinetic solutions and observations. *Lond. Edinburgh Dublin Phil. Mag. J. Sci.* **42** (281), 362–377.

TONG, F., LI, X., DUAN, Y. & YU, C. 2017 Direct numerical simulation of supersonic turbulent boundary layer subjected to a curved compression ramp. *Phys. Fluids* **29** (12), 125101.

TOWNE, A., SCHMIDT, O.T. & COLONIUS, T. 2018 Spectral proper orthogonal decomposition and its relationship to dynamic mode decomposition and resolvent analysis. *J. Fluid Mech.* **847**, 821–867.

TU, J.H. 2013 Dynamic mode decomposition: theory and applications. PhD thesis, Princeton University.

UNNIKRISHNAN, S., CAVALIERI, A.V.G. & GAITONDE, D.V. 2019 Acoustically informed statistics for wave-packet models. *AIAA J.* **57** (6), 2421–2434.

UNNIKRISHNAN, S. & GAITONDE, D.V. 2020 Linear, nonlinear and transitional regimes of second-mode instability. *J. Fluid Mech.* **905**, A25.

UNNIKRISHNAN, S. & GAITONDE, D.V. 2021 Instabilities and transition in cooled wall hypersonic boundary layers. *J. Fluid Mech.* **915**, A26.

VAN DRIEST, E.R. 1951 Turbulent boundary layer in compressible fluids. *J. Aeronaut. Sci.* **18** (3), 145–160.

VAN LEER, B. 1974 Towards the ultimate conservative difference scheme. II. Monotonicity and conservation combined in a second-order scheme. *J. Comput. Phys.* **14** (4), 361–370.

VATSA, V.N. 1995 Evaluation of a multigrid-based Navier–Stokes solver for aerothermodynamic computations. *J. Spacecr. Rockets* **32** (2), 193–199.

VATSA, V.N. & WEDAN, B.W. 1990 Development of a multigrid code for 3-D Navier–Stokes equations and its application to a grid-refinement study. *Comput. Fluids* **18** (4), 391–403.

VIARO, S. & RICCO, P. 2019*a* Compressible unsteady Görtler vortices subject to free-stream vortical disturbances. *J. Fluid Mech.* **867**, 250–299.

VIARO, S. & RICCO, P. 2019*b* Neutral stability curves of compressible Görtler flow generated by low-frequency free-stream vortical disturbances. *J. Fluid Mech.* **876**, 1146–1157.

WANNENWETSCH, G.D. & MARTINDALE, W.R. 1977 Roughness and wall temperature effects on boundary layer transition on a 0.0175-scale space shuttle orbiter model tested at Mach number 8. *Final Report ARO*.

WU, X. & CHOUDHARI, M. 2001 Effects of long-wavelength Klebanoff modes on boundary-layer instability. *Annual Research Briefs-2001* 305.

XIE, Z.T. & CASTRO, I.P. 2008 Efficient generation of inflow conditions for large eddy simulation of street-scale flows. *Flow Turbul. Combust.* **81**, 449–470.

XU, D., RICCO, P. & DUAN, L. 2024 Görtler instability and transition in compressible flows. *AIAA J.* **62** (2), 489–517.

ZAKI, T.A. & DURBIN, P.A. 2005 Mode interaction and the bypass route to transition. *J. Fluid Mech.* **531**, 85–111.

ZHANG, C. & SHI, Z. 2022 Nonlinear wave interactions in a transitional hypersonic boundary layer. *Phys. Fluids* **34** (11), 114106.

ZHOU, T., LIU, Z., LU, Y., WANG, Y. & YAN, C. 2022 Direct numerical simulation of complete transition to turbulence via first-and second-mode oblique breakdown at a high-speed boundary layer. *Phys. Fluids* **34** (7), 074101.